This is a preprint of the following article: Romei, A., & Persico, G., *Computational fluid-dynamic modelling of two-phase compressible flows of carbon dioxide in supercritical conditions*, Appl. Therm. Eng., 2021.
The published article may differ from this preprint, and is available at: 10.1016/j.applthermaleng.2021.116816

Computational fluid-dynamic modelling of two-phase compressible flows of carbon dioxide in supercritical conditions

Alessandro Romei, Giacomo Persico*

Laboratory of Fluid Machines
Energy Department, Politecnico di Milano
Via Lambruschini 4, 20156 Milano, Italy

Abstract

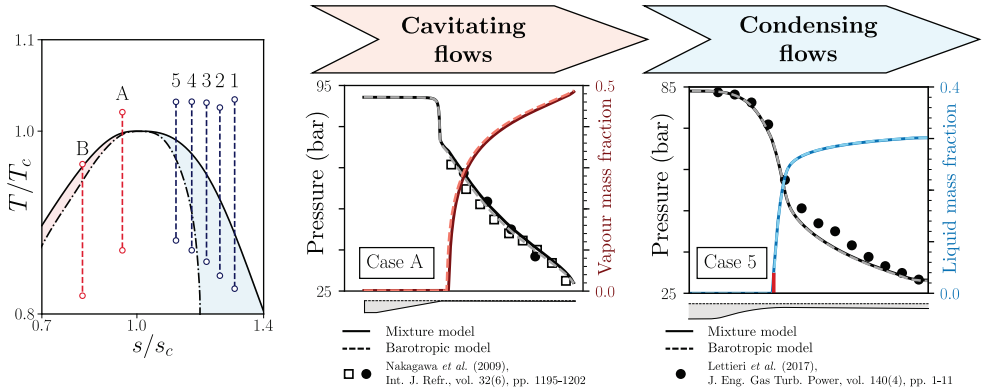

Compressible two-phase flows of carbon dioxide in supercritical thermodynamic conditions are encountered in many applications, e.g. ejectors for refrigeration and compressors for power production and carbon capture and sequestration to name a few. Alongside the phase change, transonic/supersonic flow regimes and real-gas effects also add additional complexities in the simulations of such flows. In this work, we investigate cavitating and condensing flows of carbon dioxide via numerical simulations based on the two-fluid concept, applying both a mixture model and a barotropic model. In the mixture model, the phase change is modelled with an extra transport equation for the mass of the dispersed phase and a source term introduced via a penalty formulation. The barotropic model reproduces the pressure-density relation of the mixture along the upstream isentrope. Both the models assume thermodynamic and mechanical equilibrium between phases and exclude meta-stability effects. All results are compared against experimental data taken from literature and the main numerical issues of the models are discussed in detail. The agreement between the simulations and the experiments is remarkable qualitatively and quantitatively, resulting in the range 2-4% for pressure and below 1% for temperature in terms of weighted mean absolute percentage error for supercritical expansions, even though suggesting a further margin of improvement in the physical modeling , especially for subcritical expansions. Finally, we show that the barotropic model yields comparable predictions of the expansion processes at a lower computational cost and with an improved solver robustness.

Keywords: carbon dioxide, two-phase flows, non-ideal effects, supersonic flows.

1. Introduction

Carbon dioxide (CO_2) is not only a greenhouse gas. Thanks to its low toxicity and its thermal stability for wide ranges of pressure and temperature, CO_2 (also known as R744 in the refrigeration field) is also attracting scientific research efforts and R&D investments to enable its usage as working fluid for energy systems and process engineering. Several alternative and novel energy technologies are presently based on the application of CO_2, e.g. refrigeration systems [1, 2] and closed power cycles [3, 4, 5, 6] to name a few. These technologies share a specific technical issue: in at least one component of the system, CO_2 evolves in thermodynamic states close to the critical point. An example is represented by the main compressor of closed power cycles operating with CO_2 in supercritical conditions, whose typical thermodynamic transformations are reported in the left frame of Figure 1 for the regenerative layout. The key idea behind the success of this novel power cycle is to compress CO_2 near the thermodynamic critical point, where the fluid possesses liquid-like properties. In doing so, the compression work is considerably reduced, thus increasing the useful work retrieved from the power cycle. This idea has, however, important technical implications on the device selected to compress the fluid. Due to the high fluid density, the specific speed of these machines is typically low, but not so low to justify the use of volumetric compressors [7], so turbocompressors are typically considered in supercritical CO_2 power systems. As well known, within the turbocompressor the flow undergoes severe accelerations that generate sudden local expansions, and the local thermodynamic state may fall below the saturation curve. If such condition persists for a sufficient amount of time, then the fluid can ultimately change phase, then setting the ground for two-phase flow operation within the compressor, as sketched in the right frame of Figure 1. Analogous flow features can also occur in other flow devices, which include (not exclusively) supersonic ejectors for refrigeration and valves. Interestingly, research activities in this field may also improve the economic feasibility of carbon capture and sequestration (CCS) technologies, e.g. by reducing the power consumption required by compressors or by increasing compressor operability [8].

Depending on the entropy level of the intake supercritical condition, the phase transition might lead to the formation of either vapour (when $s < s_c$) or liquid (when $s > s_c$); in other words, expanding from a general supercritical state either cavitation (liquid $\mapsto$ vapour) or condensation (vapour $\mapsto$ liquid) can take place in supercritical carbon dioxide (sCO_2) flow components. With reference to the flow devices listed above, ejectors for refrigeration typically operate for $s < s_c$, while compressors for CCS operate for $s > s_c$;

*Corresponding author
Email address: giacomo.persico@polimi.it (Giacomo Persico)

This is a preprint of the following article: Romei, A., & Persico, G., *Computational fluid-dynamic modelling of two-phase compressible flows of carbon dioxide in supercritical conditions*, Appl. Therm. Eng., 2021.
The published article may differ from this preprint, and is available at: 10.1016/j.applthermaleng.2021.116816

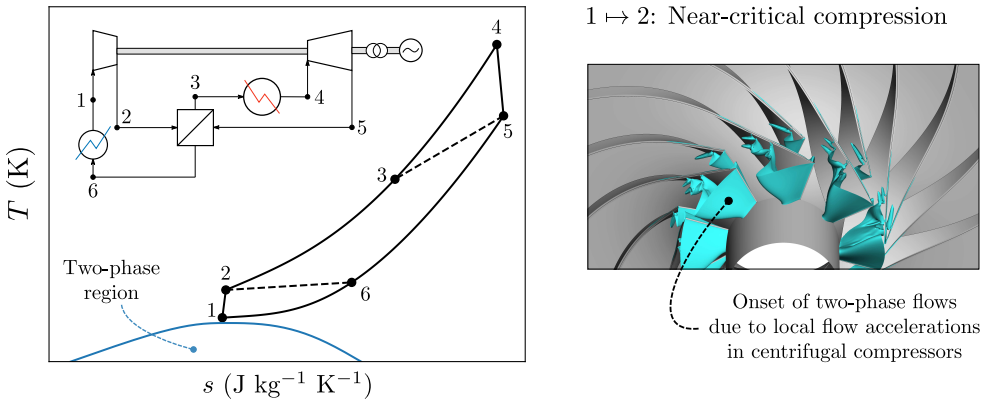

Figure 1: Representative closed power cycle based on supercritical carbon dioxide as working fluid. The compression process takes place in the neighbourhood of the critical point, hence local flow accelerations within the impeller blade channel can promote excursions below the saturation curve.

conversely, compressors for closed power cycles can be run in both the conditions, depending on the cycle configuration, the thermodynamic optimization, and the full-/part-load strategy of the plant. In all these flow devices the phase transition occurs within streams of high-speed fluid; the available experiments (see, for example, the visualization published in [9]) indicate that in such flow configurations the new phase (composed by either droplets or bubbles) appears dispersed into the main one, without evident interfaces between the phases. The onset of a dispersed phase is typically associated to a sudden drop of the speed of sound, which is comparably lower than that of the fluid in either of the saturated conditions. As a result, the onset of two-phase flows is associated to a sudden increase of the Mach number of the stream, promoting the establishment of supersonic flows, shock waves, and choking with respect to single-phase flows of the same fluid [10]. In this context, a proper computational modeling of cavitation and condensation phenomena in sCO_2 compressible flows, and their subsequent implications on the flow morphology and on the thermodynamics of the process, is crucial for the design of sCO_2 devices and, ultimately, for the technical feasibility and market penetration of the entire sCO_2 energy technology.

Two-phase flows were object of theoretical, computational and experimental studies in the last decades; historically, the vast majority of these studies was focused on water for cavitation in pumps [11] and valves [12, 13], on cryogenic fluids for rocket turbopumps [14, 15] and on steam for condensation in turbines [16, 17, 18]. The outcome of these studies is best summarized, to the authors' knowledge, in the excellent book of Brennen [19], which provides a rigorous and comprehensive presentation of two-phase flows, with emphasis on both the physical and modeling perspectives. With reference to Brennen's classification, the so-called *two-fluid model* appears to be the most computational-effective formulation to model the dispersed phase transitions of interest in this work. In the two-fluid model, the dispersed phase is considered mixed

This is a preprint of the following article: Romei, A., & Persico, G., *Computational fluid-dynamic modelling of two-phase compressible flows of carbon dioxide in supercritical conditions*, Appl. Therm. Eng., 2021.
The published article may differ from this preprint, and is available at: 10.1016/j.applthermaleng.2021.116816

from an Eulerian perspective with the main phase in a unique continuous fluid, whose mean properties are defined on the basis of proper volume or mass averages of the corresponding single-phase properties. Even within this modeling framework, several alternative sub-models were proposed in the scientific literature to treat the generation of the dispersed phase and the interaction between the phases.

The typical short time-scale of the process might allow the supercritical fluid to expand below the saturation limit without incurring in a phase change, reaching the so-called meta-stable state. Meta-stable states might exist within limited thermodynamic regions, comprised between the saturation curve (representative of the phase transition under thermodynamic equilibrium) and the spinodal curve (limit of the meta-stable equilibrium). Experiments for wet steam [20] and, recently, for sCO_2 [9] indicate that in high-speed flows the transition occurs delayed with respect to the saturation line, thus proving the existence of meta-stable states, though in limited regions of the flow. When the two phases are established, velocity and temperature differences might arise between the phases, promoting mechanical and/or thermal non-equilibrium. De Lorenzo *et al.* [21] reviewed the most relevant two-fluid models, classified them with respect to the character of non-equilibrium phenomena to be represented in the solution, and proposed a class of novel one-dimensional analytic solutions of two-phase flows in nozzles.

Such rich scientific background allows us to provide a classification of the most relevant models available for the prediction of cavitating/condensing high-speed flows, which could also be applied in presence of sCO_2 flows:

- the *homogeneous equilibrium model* (HEM), which excludes meta-stable states and assumes mechanical and thermal equilibrium between the phases;
- the *non-homogeneous equilibrium model* (NEM), which excludes meta-stable states and assumes thermal equilibrium between the phases, but allows for the existence of a relative velocity between the two phases;
- the *homogeneous frozen model* (HFM), which excludes meta-stable states and assumes mechanical equilibrium, but neglects the heat exchange between the phases;
- the *delayed equilibrium model* (DEM), which allows for the existence of meta-stable states (by considering a third phase, besides the saturated liquid and vapour, composed by the supersatured supercritical fluid), and only considers mechanical equilibrium between the phases.

Brennen [19] and De Lorenzo *el al.* [21] successfully applied these models in simple geometric configurations like ducts and nozzles, where quasi-one-dimensional analytical solutions provide a technically relevant representation of the flow. However, to pursue the thermofluid-dynamic design of the technical devices of interest for sCO_2 technology, the aforementioned models have to be reformulated in order to be implemented

This is a preprint of the following article: Romei, A., & Persico, G., *Computational fluid-dynamic modelling of two-phase compressible flows of carbon dioxide in supercritical conditions*, Appl. Therm. Eng., 2021.
The published article may differ from this preprint, and is available at: 10.1016/j.applthermaleng.2021.116816

in a multi-dimensional computational fluid-dynamic (CFD) framework. Examples of two-phase models implemented in the frame of CFD tools are reported in [22] and [23], mainly focusing on water cavitation. With respect to such studies, the supercritical condition of CO_2 complicates the thermodynamic modeling of the single phases, besides the inherent complication associated to the phase change. Recently, examples of CFD simulations of two-phase flows of sCO_2 were proposed [24, 25, 26, 27], and compared with experiments performed on either cavitating or condensing flows of sCO_2 in converging-diverging nozzles. However, in none of the aforementioned publications the proposed CFD model is compared to both classes of phase transition.

Since sCO_2 compressors for closed power cycles can operate with both lower and higher entropy than the critical one, the computational model have to be assessed for both cavitating and condensing flows. Moreover, numerical models tailored for turbomachinery design have to be robust and computationally efficient for being used in routine design and optimization tasks. To this end, we propose two alternative CFD formulations for simulating two-phase non-ideal compressible flows of sCO_2, comparing in detail their physical assumptions and numerical aspects. To cope with the large departure from the ideal-gas model, state-of-the-art thermodynamic properties are incorporated into the CFD solver via look-up-table (LUT) interpolations to speed up the calculations. LUT approaches represent the standard for simulating non-ideal flows in turbomachinery components, as widely documented in literature, see, e.g., [28, 29, 30]. Therefore, we herein focus on the multi-phase modeling; accordingly, the computational methodologies are tested on simplified converging-diverging ducts, which can effectively mimic the flow accelerations that may occur within compressor blade channels. Both cavitating and condensing flows are simulated and compared against experimental results of Nakagawa *et al.* [31] and of Lettieri *et al.* [9], respectively.

This paper is structured as follows. At first the computational models are outlined, then the two test-cases are presented. The results of the application of the flow models to, first, cavitating flows and, then, condensing flows are discussed, highlighting modeling issues and computational accuracies. Finally, a critical discussion on the calculation of the speed of sound in presence of cavitating and condensing flows is proposed.

2. Computational framework

In this section, we outline the two computational formulations that will be used throughout this work, highlighting the main modeling assumptions. Both of them stems from the two-fluid concept, but they differ in terms of the thermodynamic treatment and, ultimately, in the way in which the dispersed phase is generated and evolves within the main one. Both the flow models are implemented in the Ansys-Fluent® framework making use of ad-hoc user-defined functions (UDFs).

The first model, named *mixture model* hereinafter, considers the mixture as a whole instead of being composed by two distinct phases. Such flow modeling allows for a drastic simplification in the mathematical

This is a preprint of the following article: Romei, A., & Persico, G., *Computational fluid-dynamic modelling of two-phase compressible flows of carbon dioxide in supercritical conditions*, Appl. Therm. Eng., 2021.
The published article may differ from this preprint, and is available at: 10.1016/j.applthermaleng.2021.116816

description of the two-phase flow: the classical set of Reynolds-Average Navier-Stokes equations is recovered and formulated in terms of mixture density and mixture centre-of-mass velocity, eventually complemented with constitutive equations to model the relative motion between phases. Analogously, the energy equation is expressed in terms of the mixture enthalpy.

Defining the volumetric fraction of the main or principal phase as α_p and that of the dispersed phase as α_d, the mixture density ρ_m, molecular viscosity μ_m and thermal conductivity κ_m result from the volume-weighted average as follows:

$$\rho_m = \alpha_p \rho_p + \alpha_d \rho_d \tag{1}$$

$$\mu_m = \alpha_p \mu_p + \alpha_d \mu_d \tag{2}$$

$$\kappa_m = \alpha_p \kappa_p + \alpha_d \kappa_d \tag{3}$$

It is recalled that $\alpha_p = 1 - \alpha_d$ for single-component two-phase flow. Any specific thermodynamic quantity of the mixture ψ_m (such as enthalpy, entropy, internal energy, etc...) is instead evaluated using mass-averages, by resorting to the mass fractions of the phases. The mass fractions of the primary and dispersed phases, defined as w_p and w_d respectively, are evaluated as:

$$w_p = \frac{\rho_p}{\rho_m} \alpha_p \tag{4}$$

$$w_d = \frac{\rho_d}{\rho_m} \alpha_d \tag{5}$$

From mass conservation, the two mass fractions sum to unity, i.e. $w_p + w_d = 1$. They are used to determine the general specific mixture quantity ψ_m as follows:

$$\psi_m = w_p \psi_p + w_d \psi_d \tag{6}$$

An additional transport equation for the mass of the dispersed phase describes the generation and the evolution of the dispersed phase. The resulting set of governing equations can effectively track the evolution of averaged properties without resorting to sub-models that account for inner interactions between phases, whose modeling would require a deep knowledge of the interfacial properties [32].

The second model, named *barotropic model* hereinafter, is still based on the two-fluid flow representation and strictly assumes that (i) the phases are in thermal and mechanical equilibrium, and (ii) any thermodynamic/transport property of the mixture Ψ only depends on the pressure, e.g. $\Psi = \Psi(P)$. In general, the generic mixture property for a single-component fluid should depend on two independent thermodynamic quantities, for example $\Psi = \Psi(P, s)$. The barotropic assumption hence implies to neglect the any contribution besides the one of pressure on the quantity of interest; this means, in practice, to neglect the volumetric

This is a preprint of the following article: Romei, A., & Persico, G., *Computational fluid-dynamic modelling of two-phase compressible flows of carbon dioxide in supercritical conditions*, Appl. Therm. Eng., 2021.
The published article may differ from this preprint, and is available at: 10.1016/j.applthermaleng.2021.116816

thermal expansion of the fluid. However, thanks to the barotropic assumption the equations of motion are decoupled from the energy equation, which does not need to be explicitly resolved. Such model, though highly simplified, is deemed to be particularly relevant for turbocompressor application, since heat transfer is usually negligible in such components and the computational efficiency is crucial for their aerodynamic design and optimization.

2.1. Mixture model

The set of steady-state governing equations for the mixture model reads:

$$\begin{aligned}
\nabla \cdot (\rho_m \boldsymbol{v_m}) &= 0 \\
\nabla \cdot (\rho_m \boldsymbol{v_m} \otimes \boldsymbol{v_m}) &= \nabla \cdot (\mathcal{T} + \mathcal{T}_{turb}) - \nabla P_m \\
\nabla \cdot (\rho_m h_m^t \boldsymbol{v_m}) &= -\nabla \cdot (\boldsymbol{q} + \boldsymbol{q}_{turb}) + \nabla \cdot [\boldsymbol{v_m}(\mathcal{T} + \mathcal{T}_{turb})] \\
\nabla \cdot (\alpha_d \rho_d \boldsymbol{v_m}) &= \mathcal{G}
\end{aligned} \tag{7}$$

where no slip velocity is considered between phases, i.e. $\boldsymbol{v} = \boldsymbol{v_m} = \boldsymbol{v_p} = \boldsymbol{v_d}$, and equal pressure and temperature is assumed between the phases, i.e. $P = P_m = P_p = P_d$ and $T = T_m = T_p = T_d$, thus imposing thermal and mechanical equilibrium. The shear-stress relationship for an isotropic Newtonian fluid is supplied $\mathcal{T} = \mu_m(\nabla \otimes \boldsymbol{v_m} + (\nabla \otimes \boldsymbol{v_m})^T)$, where the contribution given by the volume viscosity coefficient is neglected in the mixture model implementation by Ansys-Fluent®. The influence of this latter contribution on compressible CO_2 flows in thermodynamic conditions of interest for this work was analysed by Fang [33], who concludes that the volume viscosity has only negligible effects on the main flow distributions. The Fourier's law $\boldsymbol{q} = -\kappa_m \nabla T_m$ is used for the heat conduction. The gross effects of turbulence, expressed by the Reynolds stresses $\mathcal{T}_{turb}$ and the turbulent heat transfer $\boldsymbol{q}_{turb}$, are introduced by means of the well-known two-equation $k-\omega$ SST model [34]. Alternatively, the turbulence effects can also be included via the one-equation Spalart-Allmaras model [35], which was proven to yield accurate predictions of the main near-wall distributions in presence of severe thermo-physical property variations [36], such as the ones across the pseudo-critical line. Expansions passing through the pseudo-critical line are not considered in this work, hence the standard $k-\omega$ SST model is employed hereinafter for the turbulence modeling. It follows that a system consisting in seven partial differential equations has to be solved for a two-dimensional problem.

The last equation of system (7) is the specific feature of the proposed mixture model and its formulation is crucial to obtain smooth numerical convergence and accurate results. The role of this equation is actually to produce a certain amount of mass-flow rate of the dispersed phase (left-hand side of the equation) when the local thermodynamic state resulting from the numerical calculation reaches the condition of phase transition by activating a mass-transfer source term $\mathcal{G}$ (right-hand side of the equation). Several formulations were proposed for this source term (see, for example, Dang *el al.*, [23], Giacomelli *el al.*, [25], Boyds *el al.*, [27]),

This is a preprint of the following article: Romei, A., & Persico, G., *Computational fluid-dynamic modelling of two-phase compressible flows of carbon dioxide in supercritical conditions*, Appl. Therm. Eng., 2021.
The published article may differ from this preprint, and is available at: 10.1016/j.applthermaleng.2021.116816

typically referring to the Hertz-Knudsen physical model [37]. In the present work, we propose a formulation similar to the one used in Hosangadi *el al.* [26] but with a different concept and implementation. We define $\mathcal{G}$ as:

$$\mathcal{G} = \mathrm{sgn}(s_0 - s_c)\,\mathcal{K}\,\left[P - P_{sat}(T)\right], \tag{8}$$

which is valid for both $P > P_{sat}(T)$, which implies condensing flows, and for $P < P_{sat}(T)$, which reproduces cavitating flows. Otherwise, $\mathcal{G} = 0$ because there is no phase change.

In our model, $P - P_{sat}(T)$ is the driving force of the phase change: when the local pressure exceeds (goes below) the saturation pressure at the local temperature, condensation (cavitation) locally occurs generating an increase in the mass of the dispersed phase. In this sense, such source term effectively mimics the Hertz-Knudsen model; however, the Hertz-Knudsen model was conceived to represent processes occurring at the microscale, which are not solved in the continuum macroscopic framework of the CFD. Hence, we just retain the general intuition to construct the mathematical model: from the mathematical perspective, this formulation is actually a *penalty* term introduced in the equation to numerically impose the satisfaction of a constraint, i.e. the onset of transition when $P = P_{sat}(T)$. As a matter of fact, under the assumption of a stable thermodynamic equilibrium, the last equation of the mixture model would be redundant if the CFD code uses either two specific or one specific and one intensive thermodynamic variables as primitive variables. Nonetheless, when using two intensive thermodynamic quantities, such as pressure and temperature as in the present work, there is the need to impose a constraint on those two variables to guide the solution towards thermodynamic equilibrium, i.e. $P = P_{sat}(T)$ Therefore, the numerical difference $P - P_{sat}(T)$ can be interpreted as a violation of the stable thermodynamic equilibrium and it becomes an artificial effect of the penalty formulation. To control $P - P_{sat}(T)$, and thus recovering an accurate numerical approximation of the two-phase solutions, i.e. $P \approx P_{sat}(T)$, the formulation of $\mathcal{G}$ features the penalty coefficient $\mathcal{K}$ $[\mathrm{s\,m^{-2}}]$, which is dimensional and represents the weight of the penalty: the higher the $\mathcal{K}$, the lower $P - P_{sat}(T)$. In the result section, we will show the influence of this parameter on the accuracy of the solutions. From the analytical perspective, the optimal choice of the penalty coefficient would be $\mathcal{K} \mapsto \infty$ to have infinitesimal constraint violations. However, in the numerical context such a choice would cause convergence issues, because even a negligible violation of the constraint would dramatically affect the numerical value of the source term $\mathcal{G}$. Hence, the correct choice of $\mathcal{K}$ has to ensure a smooth convergence process alongside a negligible violation of the constraint, in the limit of the approximation of the numerical solution. It is only anticipated that $\mathcal{K} = \mathcal{O}(10^2 \div 10^3)\,\mathrm{s\,m^{-2}}$ is sufficient to impose that, in the two-phase region of the flow, the solution links the pressure field with the temperature field such that the actual P approximates $P_{sat}(T)$ with a small numerical error ($< 0.5\%$).

It is also worth mentioning that the present interpretation is fundamentally different from that of Dang

This is a preprint of the following article: Romei, A., & Persico, G., *Computational fluid-dynamic modelling of two-phase compressible flows of carbon dioxide in supercritical conditions*, Appl. Therm. Eng., 2021.
The published article may differ from this preprint, and is available at: 10.1016/j.applthermaleng.2021.116816

et al. [23], in which the pressure difference is assigned a priori, Hosangadi *et al.* [26], in which the equilibrium condition $P = P_{sat}(T)$ is not recovered in the solution, and Bodys *et al.* [27], in which a reference saturation pressure is defined and the source term monotonically increases along the expansion accordingly. In the present set-up, the source term is not representative of any physical considerations regarding thermal, mechanical or thermodynamic equilibrium, but only represents a mathematical expedient to enforce equilibrium conditions when using two intensive variables as primitive variables in the CFD solver.

As a final note on the source term formulation, in this work the phase transition was set at the saturation, hence it was assumed that the fluid undergoes an instantaneous phase change. Under these circumstances, the mixture model (with negligible violation of the constraint) corresponds to a HEM formulated in a CFD framework, making use of pressure and temperature as primitive variables. However, depending on local thermodynamic conditions, a finite time is required to complete the phase-change process, exhibiting meta-stable states in the meantime. If a reliable expression of the Wilson line is available for the process of interest, the Wilson line might be specified to set the limit at which stable thermodynamic equilibrium is recovered, while separately modeling the meta-stable fluid, e.g. in a DEM fashion.

2.1.1. Thermodynamic modeling

A further issue of the mixture model, particularly relevant to sCO_2 application, is the thermodynamic modeling of the supercritical fluid in the single-phase region and of the individual phases in the two-phase region. Due to the near-critical conditions, a generalized thermodynamic description is required. In the present formulation, any generic property Ψ of the single-phase primary phase (when either $P > P_c$, $T > T_c$ or $P > P_{sat}(T)$ if the primary phase is liquid or $P < P_{sat}(T)$ if the primary phase is vapour) is expressed as a function of pressure and temperature, i.e. $\Psi_p = \Psi_p(P, T)$. A LUT approach was implemented in Ansys-Fluent® and supplied via a user-defined real-gas model (UDRGM). Following this approach, discrete values of each thermodynamic property are stored in a tabular form assuming uniform steps in pressure and temperature, as sketched in Figure 2(a). An uniform step allows for a faster search of the stored values at a generic location. As a drawback, the memory requirements is generally higher, because the inability to have localized refinements close to the critical point asks for larger tables, as the uniform step is dictated by the region in which the gradients in thermodynamic properties are higher. However, we rather preferred to reduce the cost of the single CFD iteration over a reduced memory requirement. The value of Ψ_p at a generic pair (P, T) is then computed with a bilinear interpolation between the four closest thermodynamic nodes. Although meta-stable states are not simulated in the present work, the thermodynamic tables are built by extrapolating the single phase properties until the corresponding spinodal limit to increase the margin from the discontinuous liquid-vapour change in thermodynamic properties, as exemplary reported in Figure 2(b) for the density. Such expedient allows keeping the bilinear interpolation even in close proximity of the saturation curve, where one or more of the closest nodes may fall behind the saturation line but still

This is a preprint of the following article: Romei, A., & Persico, G., *Computational fluid-dynamic modelling of two-phase compressible flows of carbon dioxide in supercritical conditions*, Appl. Therm. Eng., 2021.
The published article may differ from this preprint, and is available at: 10.1016/j.applthermaleng.2021.116816

(a) Example of LUT discretization (7×7)

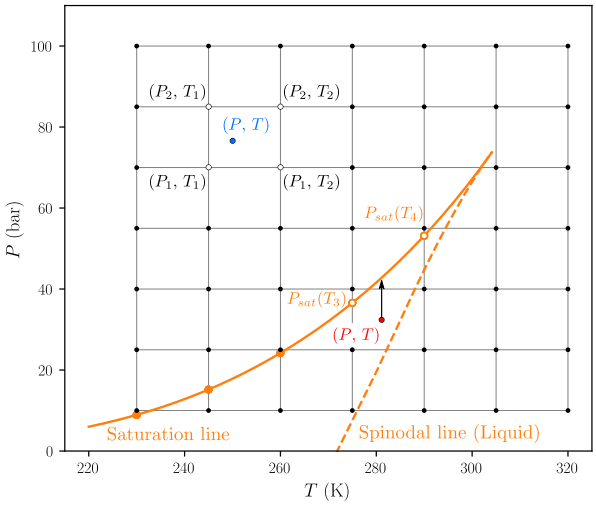

(b) Example of thermodynamic property, $\Psi = \rho$

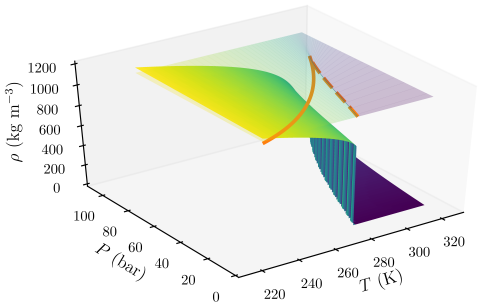

(c) Bilinear Interpolation
$P > P_{sat}(T)$ (cavitation) or $P > P_c$ or $T > T_c$

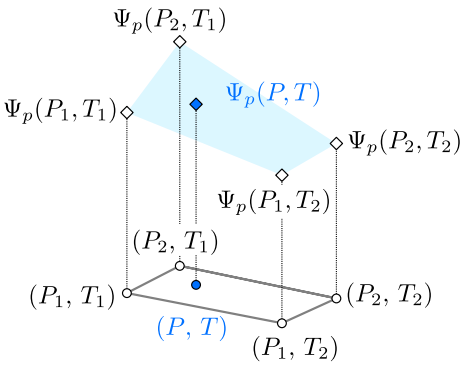

(d) Linear Interpolation
$P \leq P_{sat}(T)$ (cavitation) and $P \leq P_c$ and $T \leq T_c$

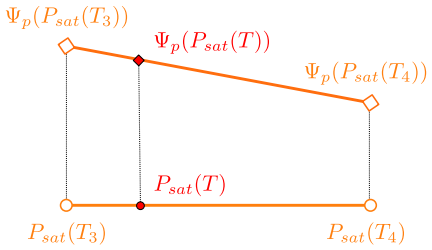

Figure 2: Schematic representation of the LUT approach implemented within the mixture model for the thermodynamic modeling of the primary phase. For illustrative purposes, the primary phase is considered as a liquid and the phase transition is cavitation (liquid-to-vapour), but the opposite scenario (vapour as primary phase and condensation as phase-change phenomenon) follows the same conceptual steps. The LUT for the secondary phase only involves the linear interpolation.

within the meta-stable region. If an interpolating point falls behind the spinodal line (as it happens in the close proximity of the critical point, where the meta-stable region is narrowed), its value is set equal to the saturation one. A schematic representation of the bilinear interpolation is reported in Figure 2(c).

When the primary phase is in equilibrium with the dispersed phase (when $P < P_{sat}(T)$ if the primary phase is liquid or $P > P_{sat}(T)$ if the primary phase is vapour), Ψ_p is only function of the saturation pressure at the local temperature, i.e. $\Psi_p = \Psi_p(P_{sat}(T))$. The local properties are thus computed with a linear interpolation as in Figure 2(d) between the two closest saturation nodes (orange dots in Figure 2(a)), which are determined by sampling the saturation line at the subcritical temperature locations. In practice, an if-statement discriminates between the two interpolation schemes in the developed UDRGM.

This is a preprint of the following article: Romei, A., & Persico, G., *Computational fluid-dynamic modelling of two-phase compressible flows of carbon dioxide in supercritical conditions*, Appl. Therm. Eng., 2021.
The published article may differ from this preprint, and is available at: 10.1016/j.applthermaleng.2021.116816

On the other hand, the dispersed phase can only exist in equilibrium with the primary one, hence the thermodynamic properties are always expressed as a function of the saturation pressure only, i.e. $\Psi_d = \Psi_d(P_{sat}(T))$. Therefore, the thermodynamic properties of the dispersed fluid are implemented with a standard UDF, which contains only the linear interpolation scheme discussed for the primary phase and reported in Figure 2(c). It is worth mentioning that the dispersed-phase properties are functions of only one independent variable (temperature), which unequivocally determines the local saturation pressure on which the interpolation is performed.

For both phases, the thermodynamic tables are generated by making use of Refprop®, which implements a multi-parameter equation of state expressed in terms of the Helmholtz fundamental relation [38] for CO_2. Transport properties μ, κ are computed in analogy with the thermodynamic properties, employing the relationships made available by Refprop® in the construction of the tables. Overall, full P–T tables are generated for the primary phase, while saturation tables are generated for both phases. The resulting mixture properties follow the averaging procedures described in §2.

The accuracy of the LUT interpolation is verified by considering a quasi-one-dimensional isentropic flow with constant total enthalpy $h^t = h(P^t = 91\,\text{bar}, T^t = 310.45\,\text{K})$. The selected upstream total state is the closest to the critical point among all two-phase flows that will be investigated in this work, thus representing the most challenging case for the LUT testing. The associated entropy level is $s/s_c = 0.95$, hence the primary phase is liquid while the dispersed phase is vapour. The sampled thermodynamic region is $[230\,\text{K}, 320\,\text{K}] \times [10\,\text{bar}, 100\,\text{bar}]$ and three different grid refinements are considered, namely 601×601, 1201×1201 and 2401×2401. LUT predictions are compared against Refprop® estimates in Figure 3 for density, enthalpy and molecular viscosity. For all grid refinements, the largest discrepancy is found for the primary phase in the proximity of the phase-change onset. The coarsest table returns an absolute error of 1.3%, which decreases to 0.2% for the most refined table. Within the two-phase region, where the properties are only functions of the saturation pressure, the maximum error is about 0.1% regardless of the LUT refinement. Therefore, thermodynamic tables 2401×2401 are selected for the following analyses.

2.2. Barotropic model

The set of steady-state governing equations for the barotropic model reads:

$$\begin{aligned} \nabla \cdot (\rho \boldsymbol{v}) &= 0 \\ \nabla \cdot (\rho \boldsymbol{v} \otimes \boldsymbol{v}) &= \nabla \cdot (\mathcal{T} + \mathcal{T}_{turb}) - \nabla P \end{aligned} \tag{9}$$

The two-equation $k - \omega$ SST model [34] completes the system of governing equations by taking into account turbulence effects.

The barotropic set of equations are simply the single-phase Reynold-Averaged Navier-Stokes equations, in which the fluid behaves like the mixture when the thermodynamic state falls below the saturation curve.

This is a preprint of the following article: Romei, A., & Persico, G., *Computational fluid-dynamic modelling of two-phase compressible flows of carbon dioxide in supercritical conditions*, Appl. Therm. Eng., 2021.
The published article may differ from this preprint, and is available at: 10.1016/j.applthermaleng.2021.116816

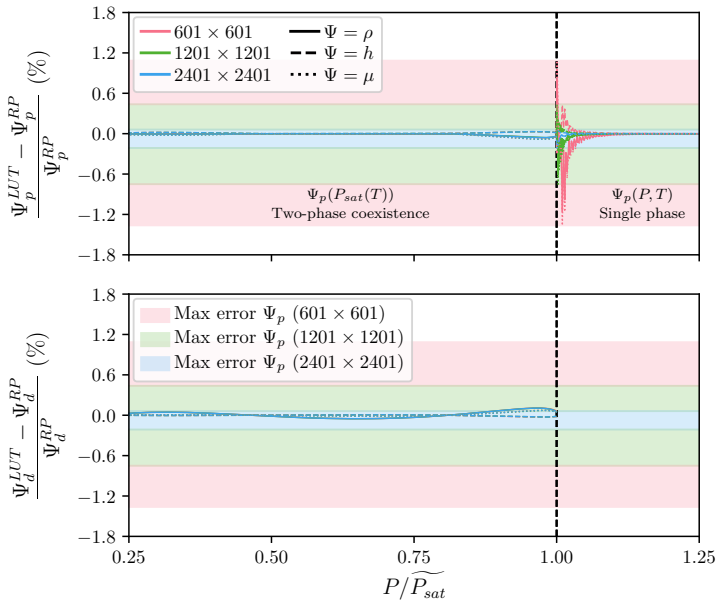

Figure 3: Errors of different LUT discretizations against Refprop® predictions in density, enthalpy and molecular viscosity estimates for an isentropic cavitating flows at constant total enthalpy $h^t = h(P^t = 91\,\text{bar}, T^t = 310.45\,\text{K})$ (labelled as case A later in the manuscript). The coloured bands show the maximum error found in the thermodynamic description of the primary phase for the given LUT discretization.

Compared to the mixture model, the barotropic formulation inherently excludes any mechanical or thermal disequilibrium between phases, and hence it strictly belongs to the HEM class. Furthermore, the barotropic assumption implies that the thermo-physical properties of the fluid, which should depend on two thermodynamic quantities, are only dependent on pressure, thus neglecting any thermal effect: the fluid is therefore considered compressible but not thermally expandable, i.e. $(\partial\rho/\partial P)_T \neq 0$ and $(\partial\rho/\partial T)_P = 0$ respectively. Such assumption simplifies the resulting flow representation with respect to the classical HEM (whose most general formulation is reported, for example, in [24]), but it provides crucial advantages from the computational perspective. The barotropic model decouples mechanical from thermal effects, removing the need of solving the energy equation to characterize the thermo-physical fluid properties. As a consequence, the mathematical problem is reduced to the resolution of five partial differential equations (for 2D systems), two less than the mixture model. Moreover, the solver becomes inherently more robust than mixture model when dealing with supercritical fluids, because it does not handle the sharp gradients of c_P which arise close to the critical point (wherein c_P is singular). In a hierarchy of CFD models, the barotropic model is therefore the most robust and computationally efficient numerical formulation which can be conceived for tackling the numerical simulation of multi-dimensional two-phase flows of sCO_2.

The physical accuracy of the model strongly relies on the definition of the barotropic relationships for

This is a preprint of the following article: Romei, A., & Persico, G., *Computational fluid-dynamic modelling of two-phase compressible flows of carbon dioxide in supercritical conditions*, Appl. Therm. Eng., 2021.
The published article may differ from this preprint, and is available at: 10.1016/j.applthermaleng.2021.116816

the three thermo-physical properties of interest for the solution, i.e. the density, the molecular viscosity and the speed of sound c:

$$\begin{aligned} \rho &= \rho(P) \\ \mu &= \mu(P) \\ c &= c(P) \end{aligned} \tag{10}$$

Since these properties physically depend also on entropy, a choice on the entropy generation across the process has to be made to obtain the three relationships (10). An obvious possibility, considered in the simulations reported in this work, is to keep the entropy level constant at the upstream value $s = s_0$. This choice physically means that the thermal effects prompted by the entropy generation on the aforementioned properties are ignored. It is worth stressing that the choice of building barotropic relationships based on the upstream entropy does not mean to assume isentropic flows: the mechanical dissipation is indeed introduced via viscous and turbulent effects in the momentum equation; the model simply ignores the correction to the thermo-physical properties due to this dissipation, which would cause an increase of entropy. However, if a preliminary estimate on the entropy generation across the process is available, as often occurs for turbocompressor simulations (via the estimated aerodynamic efficiency, for example), the barotropic relations (10) could be in principle constructed considering the estimated entropy rise, thus refining the thermodynamic accuracy of the solution. In the results section we will discuss the contribution given by the entropy generation, by comparing the results of the mixture model with that of the barotropic models.

As barotropic relationships only depend on a single independent variable, a LUT approach based on the linear interpolation scheme described in §2.1.1 is encoded in a dedicated UDF. Tabular values for ρ, μ and single-phase c are computed via Refprop®, while different formulations for c in the two-phase region are tested and discussed in the last section of the manuscript. However, the choice of the two-phase speed of sound does not alter the obtained flow solutions, as the actual value only depends on the governing equations that are solved [39, 25]. Consistently with the mixture model, the tabular properties are generated in the pressure interval $[10\,\text{bar}, 100\,\text{bar}]$ with a step of $3.75 \times 10^{-2}\,\text{bar}$.

3. Reference two-phase expanding flows

We here introduce the reference cases against which the two numerical models are validated. Since both the computational strategies focus on the mixture evolution, in principle there should be no differences among cavitating and condensing flows regardless of the phase change initialization. However, despite the generality of the mathematical formulation, the adequacy of the simulation tools in properly representing the macroscopic flow features of two-phase compressible flows has to be verified for both flow conditions.

This is a preprint of the following article: Romei, A., & Persico, G., *Computational fluid-dynamic modelling of two-phase compressible flows of carbon dioxide in supercritical conditions*, Appl. Therm. Eng., 2021.
The published article may differ from this preprint, and is available at: 10.1016/j.applthermaleng.2021.116816

Specifically, we considered the experiments made by Nakagawa *et al.* [31] to validate the computational solver for CO_2 cavitating flows and the experimental data provided by Lettieri *et al.* [9] for the validation of CO_2 condensing flows. For both experiments, the nozzle width is large enough compared to the nozzle height such that three-dimensional effects are expected to be negligible. Therefore, two-dimensional simulations are carried out for both cavitating and condensing flows.

Nakagawa *et al.* [31] analysed cavitating flows of CO_2 for several converging-diverging nozzle geometries, featuring different divergence angles, and for different upstream total conditions. They provided pressure and temperature measurements along the nozzle axis by means of pressure transducers and thermocouples. Specifically, four strain-gauge taps and nine thermocouple taps were distributed along the diverging section of the nozzle. Comparing pressure and temperature measurements in the two-phase region, Nakagawa *et al.* argued that stable thermodynamic equilibrium is established very soon in the diverging section. In the present work, we focused on the nozzle geometry with a divergence angle of 0.153° for the two published upstream total conditions. Based on the isentropic homogeneous theory, the authors claimed that the flow regime is not supersonic for both expansion processes. This conjecture will be object of a specific analysis in the final part of the present paper. Authors also pointed out that a supersonic flow regime was established for nozzle geometries with a higher divergence angle, but the measured pressure falls below the triple point. To avoid dealing with three-phase flows, these latter cases are not considered in this work.

Lettieri *et al.* [9] performed five supersonic expansions at $s > s_c$ whose upstream total state progressively approaches the thermodynamic critical point. They provided the pressure evolution along the nozzle, measured with pressure transducers at several (13) nozzle axial locations; moreover, through an optical apparatus, they also obtained visualizations of the two-phase flows inside the converging-diverging nozzle as well as the experimental condensation onset for each condition. They showed that all expansion processes are characterized by a misty flow regime, where the two phases are practically indistinguishable [9, Fig. 9]. By virtue of such experimental observations, a mixture description of the two-phase flow according to the two-fluid model appears an appropriate approximation.

Table 1 reports the boundary conditions for the cavitating and condensing flows that will be discussed in this work along with the upstream entropy level. Cavitating flows are denoted with a capital letter, while condensing flows are identified by a number. In Figure 4 the corresponding isentropic processes in the T–s thermodynamic plane are reported. Out of the seven conditions available from experiments, case A, case 4 and case 5 are expansions evolving from a supercritical upstream state ($T > T_c$ and $P > P_c$). As a final note, the shaded areas in Figure 4 represent the extent of the meta-stable region predicted by the multi-parameter equation of state included in the Refprop®. As already stated, in constructing the CFD models the onset of phase change was set at the saturation, thus excluding any meta-stability effects. The plot shows that the extent of the meta-stable regions progressively reduces when approaching the critical point, suggesting a minor relevance of meta-stable effects for cases evolving in near-critical conditions, i.e.

This is a preprint of the following article: Romei, A., & Persico, G., *Computational fluid-dynamic modelling of two-phase compressible flows of carbon dioxide in supercritical conditions*, Appl. Therm. Eng., 2021.
The published article may differ from this preprint, and is available at: 10.1016/j.applthermaleng.2021.116816

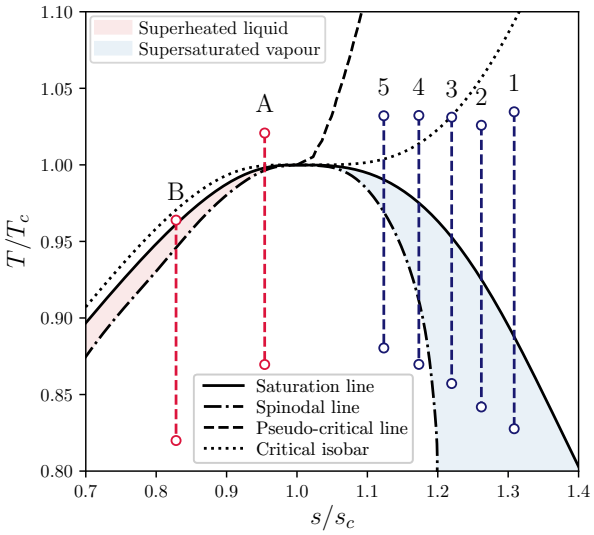

Figure 4: Reference isentropic expansions that are considered in this work for the validation of the proposed computational methodologies.

case A and case 5 and 4 for cavitating and condensing flows, respectively. These three cases are also the only ones, among the tested conditions, for that the expansion evolves from a supercritical state, thus being the most representative of the local expansions occurring in sCO_2 compressors. Therefore, cases A, 5, and 4 are the most relevant for the present study.

Table 1: Summary of boundary conditions for the cavitating (labelled with a capital letter) and condensing (labelled with a number) flows simulated in this work. For condensing flows, the outlet static pressure is not specified because its value is ignored as a consequence of the supersonic flow regime.

Case	P_0^t (bar)	T_0^t (K)	P_1 (bar)	s_0/s_c
A	91.00	310.45	27.5	0.95
B	61.00	293.15	17.5	0.83
1	58.96	314.67	-	1.31
2	65.35	311.99	-	1.26
3	73.53	313.60	-	1.22
4	79.99	313.94	-	1.17
5	84.74	313.88	-	1.12

This is a preprint of the following article: Romei, A., & Persico, G., *Computational fluid-dynamic modelling of two-phase compressible flows of carbon dioxide in supercritical conditions*, Appl. Therm. Eng., 2021.
The published article may differ from this preprint, and is available at: 10.1016/j.applthermaleng.2021.116816

4. Results

4.1. Cavitating flows

We first consider the case of cavitating flow, occurring when the inlet entropy level is lower than the critical one; such condition is representative of the local expansions occurring in the intake region of the main compressor of sCO_2 closed power cycles [40]. In this context, when the phase transition takes place the primary phase is liquid and the dispersed one is vapour, hence $\alpha_p = \alpha_L$ and $\alpha_d = \alpha_V$. The phase change occurs when $P < P_{sat}(T)$.

Total pressure and total temperature are prescribed at the inlet section as in Table 1 for the two expansion processes considered, imposing $\alpha_V = 0$ therein (the flow enters only in liquid phase). For the barotropic model, only the total pressure is specified. As for the turbulent boundary conditions, a hydraulic diameter equal to 10.0 mm (i.e., twice the height of the inlet section) and an eddy viscosity ratio equal to 2.5 are assigned, representative of a low turbulence level as expected in a nozzle expanding flow from a reservoir; the algorithms implemented in Ansys-Fluent® obtain the corresponding values of k and ω assigned at the inlet. The static pressure is specified at the nozzle outlet as in Table 1. However, it is to be noted that if a supersonic condition is reached at the nozzle outlet, the solver ignores the assigned pressure value and calculates the proper adapted pressure value.

No-slip and adiabatic boundary conditions are prescribed at the wall, which is not considered smooth. As reported in [41], a mean roughness of 2 µm is considered on the nozzle wall; this value is converted into an equivalent sand-grain roughness using a conversion factor of 3.1 [42], resulting in $k_s = 6.2\,\mu$m. Even though it might appear very small in absolute terms, the relevance of the wall roughness stems from the small scale of the experiment. A comparison with results obtained assuming smooth surfaces will be proposed later in this Section, when discussing the aerodynamics of the nozzle. Finally, a symmetry condition is imposed at the nozzle axis.

The system of equations for the mixture model is solved in the following order: the continuity and the momentum equations are solved together in a coupled fashion, then energy equation, vapour-mass equation and turbulence equations are solved separately in this order. The barotropic model makes use of the same resolution scheme, but energy and vapour-mass equations are not solved. All equations are discretised with a third-order QUICK scheme for both models. Furthermore, the PRESTO! scheme is used to interpolate the pressure at the cell face, while the gradient is reconstructed with a Green-Gauss node-based technique.

A grid convergence assessment is first carried out by generating three hexahedral grids with an increasing number of elements, by taking as a reference the case A. The mixture model is considered for this mesh analysis but equivalent outcomes are found for the barotropic simulations as well. In increasing the mesh resolution, the number of elements are doubled each time in the x-direction while keeping the same wall resolution, i.e. 9 evenly spaced layers in the y-direction with a first-layer wall distance equal to 6.7×10^{-6} m

This is a preprint of the following article: Romei, A., & Persico, G., *Computational fluid-dynamic modelling of two-phase compressible flows of carbon dioxide in supercritical conditions*, Appl. Therm. Eng., 2021.
The published article may differ from this preprint, and is available at: 10.1016/j.applthermaleng.2021.116816

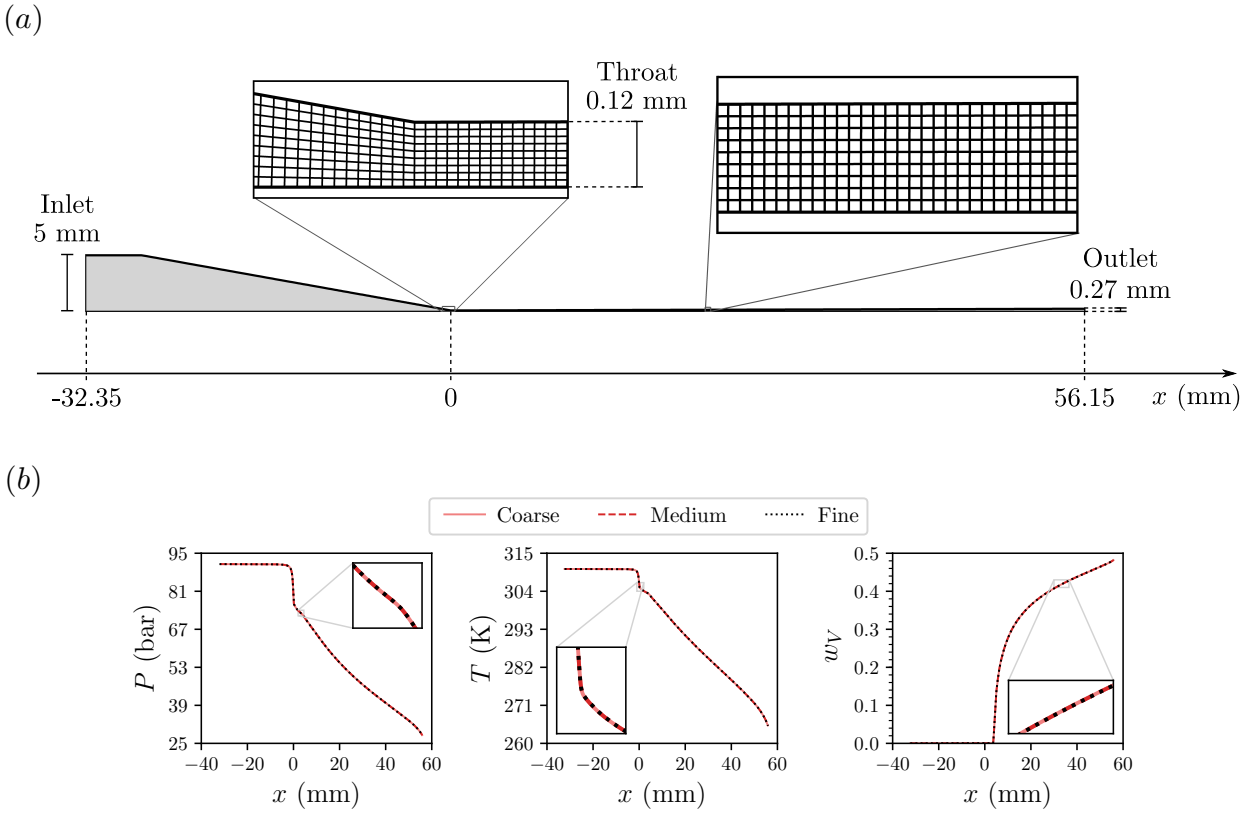

Figure 5: Grid-convergence assessment for cavitating-flow simulations: (*a*) the medium mesh selected as the grid-independent mesh (number of elements $\approx 3 \times 10^4$, grid resolution at the throat 2×10^{-5} m, 9 evenly spaced elements along the y-direction with a first-layer wall distance at the throat of 6.7×10^{-6} m) alongside the main nozzle dimensions, (*b*) pressure, temperature and vapour-mass fraction distributions for different grid refinements. The grid convergence study is performed on case A.

at the throat. The number of elements along the y-direction is dictated by the selected surface roughness, i.e. the first centre-cell distance has to be higher than the roughness value.

The results of this study in terms of main flow distributions is reported in Figure 5, showing that only minor differences are found among three meshes with increasing number of elements. The geometrical error is also quantified by computing the grid convergence index (GCI) at five axial location along the diverging section of the nozzle for pressure, temperature and liquid mass fraction. The GCIs is evaluated by estimating the apparent order of convergence as outlined in Roache [43]. The GCIs between the medium and the fine mesh for the above quantities of interest are reported in Table 2, showing that the maximum error is around 0.01%. The same error is also found when estimating the GCI for the mass-flow rate, demonstrating that a complete grid convergence is achieved for the medium mesh. Therefore, the medium mesh is selected for the following analyses, consisting in overall $\approx 3 \times 10^4$ elements, with a grid resolution at throat of 2×10^{-5} m. The aspect ratio is included between 1.4 and 2. The selected computational mesh is displayed in Figure

This is a preprint of the following article: Romei, A., & Persico, G., *Computational fluid-dynamic modelling of two-phase compressible flows of carbon dioxide in supercritical conditions*, Appl. Therm. Eng., 2021.
The published article may differ from this preprint, and is available at: 10.1016/j.applthermaleng.2021.116816

Table 2: Grid convergence indexes for pressure, temperature and vapour-mass fraction at selected axial locations along the diverging section. The grid-convergence study is performed on case A.

	GCI		
x (mm)	P (%)	T (%)	w_V (%)
0	0.01	0.00	0.00
15	0.00	0.00	0.00
30	0.00	0.00	0.00
45	−0.01	0.00	0.00
55	−0.01	0.00	0.00

5(a).

As a final and most relevant modeling issue, the setting of the penalty term $\mathcal{G}$ in the mixture model is defined though a set of simulations featuring progressively higher values of the penalty constant $\mathcal{K}$, whose value is raised from $10\,\mathrm{sm}^{-2}$ to $10^3\,\mathrm{sm}^{-2}$. The results of three calculations are reported in Figure 6 in terms of pressure distributions (left) and vapour mass fraction (right). Simulation results denote an evident convergence process, showing significant differences when the penalty parameter is raised from $10\,\mathrm{sm}^{-2}$ to $10^2\,\mathrm{sm}^{-2}$, while nearly identical profiles are predicted when $\mathcal{K}$ is raised from $10^2\,\mathrm{sm}^{-2}$ to $10^3\,\mathrm{sm}^{-2}$. For these values of $\mathcal{K}$, the constraint $P - P_{sat}(T)$ is violated with a maximum error of 0.5% in the early stages of the phase transitions, which is also the region most affected by the penalty coefficient. The error is then reduced of one order of magnitude in the ongoing expansion. Higher values of $\mathcal{K}$ interfered with the convergence process, as small violations of the constraint provoked an extremely large source term, thus preventing from achieving a stable convergence. From the results of this analysis, $\mathcal{K} = 10^3\,\mathrm{s\,m}^{-2}$ is systematically set in all following simulations performed with the mixture model.

After the definition of the numerical set-up, we now focus on the experimental assessment of the CFD models. Simulation results are compared against experimental data [31] for both cases A and case B in Figure 7 in terms of pressure and temperature profiles along the nozzle axis. As in the experimental reference, temperature measurements are also converted in pressure values through Refprop® assuming stable thermodynamic conditions, i.e $T_{exp} \mapsto P_{exp} = P_{sat}(T_{exp})$. For all cases the deviations between numerical models and the experimental data are quantified and reported in a tabular form in Appendix A.

First considering case A, the agreement between the predicted pressure trends and the experimental one is excellent with both the direct or indirect pressure measurements. The maximum relative deviation, defined as $\varepsilon = (P_{mix} - P_{exp})/P_{exp}$, is located at the last pressure tap and amounts to 8.5%. The temperature distribution predicted by the mixture model is also compared with the experimental temperature data,

This is a preprint of the following article: Romei, A., & Persico, G., *Computational fluid-dynamic modelling of two-phase compressible flows of carbon dioxide in supercritical conditions*, Appl. Therm. Eng., 2021.
The published article may differ from this preprint, and is available at: 10.1016/j.applthermaleng.2021.116816

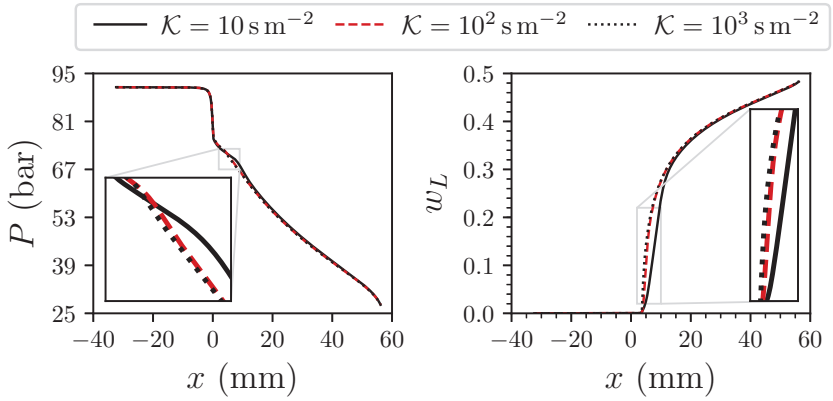

Figure 6: Influence of the penalty constant $\mathcal{K}$ on the solution of the case A.

returning a maximum deviation of 1.3% found at the last thermocouple.

Apart from local deviations, the introduction of a single parameter that summarizes the deviation of numerical predictions with respect to experiments can be useful to evaluate the overall quality of the numerical model. In the forecasting field, the weighted mean absolute percentage error (WMAPE) is widely used to quantify the quality of a forecast. Whether X is pressure or temperature, this error can be formulated as:

$$\mathrm{WMAPE}(X) = \frac{\sum_i |X_{exp,i} - X_{mix,i}|}{\sum_i X_{exp,i}} \cdot 100 \quad [\%] \tag{11}$$

Applied to the case A, the error is 2.2% and 0.7% for pressure and temperature, respectively.

The agreement with the experimental data drops when considering the non-supercritical case B, for that a systematic over-prediction affects the expansion, although the overall trend is properly reproduced. The overprediction of the experimental data by the mixture model is contained between 11.5% (second pressure tap) and 35.8% (last pressure tap) for the pressure measurements. One order of magnitude smaller deviations are, instead, found for temperature measurements, whose maximum discrepancy amounts to 3.0% in correspondence of the last thermocouple. The overall deviation from pressure and temperature trends, following the definition provided in Eq. 11, is 23.1% and 2.1%, respectively. One possible explanation for such larger deviations is that meta-stable effects, negligible close to the critical point as in case A ($s/s_c = 0.95$), gain importance away from it as in case B ($s/s_c = 0.83$). Such differences are consistent with the results of Palacz *et al.* [24], who also found a reduction in the HEM accuracy away from the critical point. However, a closer inspection of the experimental data for case B shows a certain scattering of the experimental pressure data, especially between direct and temperature-derived measurements. In particular, towards the end of the divergent the predicted pressure profile qualitatively follows the trend established by temperature and associated pressure data; in this region, relatively far from any potential delay introduced by meta-stable effects, conditions of stable thermodynamic equilibrium should have been recovered.

This is a preprint of the following article: Romei, A., & Persico, G., *Computational fluid-dynamic modelling of two-phase compressible flows of carbon dioxide in supercritical conditions*, Appl. Therm. Eng., 2021.
The published article may differ from this preprint, and is available at: 10.1016/j.applthermaleng.2021.116816

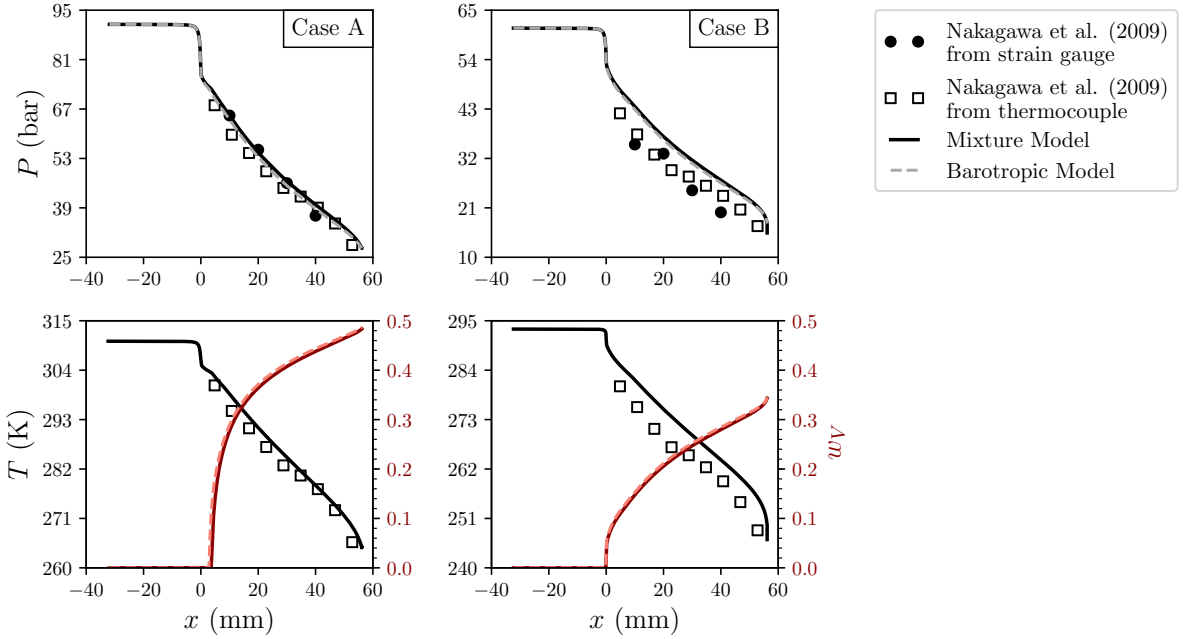

Figure 7: Comparison of the mixture (solid lines) and barotropic (dashed lines) model against experimental data [31] along the nozzle axis. The vapour-mass fraction predicted by the barotropic model is computed as a post-processing.

The above considerations apply identically for both the mixture and the barotropic models, which exhibit qualitatively equal predictions in terms of pressure profiles. Quantitatively, the maximum deviation between mixture and barotropic estimates is 2.9% and 2.3% for case A and case B, respectively. However, the thermodynamic implications of the simplified barotropic assumption are interesting to investigate and, hence, a detailed post-processing was performed on the computed data to obtain estimates for:

- the enthalpy field, as $h_{baro} = h(P_0^t, T_0^t) - 0.5 \cdot v_{baro}^2$
- the entropy field, as $s_{baro} = s(P_{baro}, h_{baro})$
- the vapour mass-fraction, as $w_{V,baro} = w_V(P_{baro}, h_{baro})$

These thermodynamic estimates can be performed straightforwardly if the total enthalpy is assumed uniform over the entire flow field. This assumption is actually a simplification of the actual flow configuration: even if the nozzle walls are adiabatic, implying that the flux of total enthalpy must be conserved, local gradients of the total enthalpy might arise as a consequence of internal heat-transfer processes between layers of fluid at different temperature. One classical example is the heat transfer between the boundary layer, heated by the viscous dissipation, and the adjacent free-stream region. The mixture model, by virtue of its complete thermodynamic formulation and its agreement with the experimental temperature profile, can be used as a benchmark for the aforementioned processing of barotropic-simulation data.

This is a preprint of the following article: Romei, A., & Persico, G., *Computational fluid-dynamic modelling of two-phase compressible flows of carbon dioxide in supercritical conditions*, Appl. Therm. Eng., 2021.
The published article may differ from this preprint, and is available at: 10.1016/j.applthermaleng.2021.116816

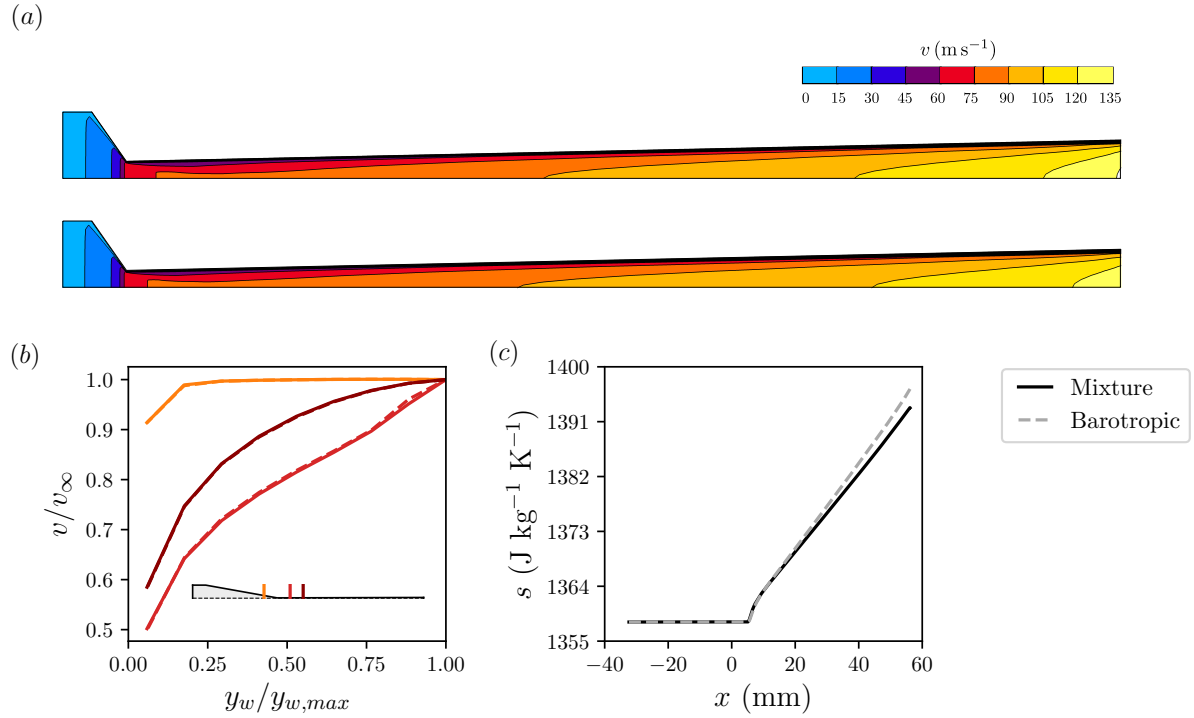

Figure 8: (a) Velocity fields predicted by the mixture model (top) and barotropic model (bottom) for the case A For visualization purposes, the x-direction is stretched such that $x/y = 0.125$ and the convergent section is not shown; (b) spanwise velocity profiles for three relevant sections, namely at $x = -5\,\mathrm{mm}$ (orange lines), $5\,\mathrm{mm}$ (red lines) and $10\,\mathrm{mm}$ (dark-red lines); (c) entropy distributions along the nozzle axis for the mixture and the barotropic model.

Figure 8 summarizes significant flow features predicted for the supercritical condition of case A. It reports the two-dimensional distributions of the velocity magnitude, as well as spanwise velocity profiles for three relevant sections across the throat, and the entropy distribution along the nozzle axis. For each of these plots, results obtained with the mixture model (solid lines) are compared with corresponding data extracted/processed from the barotropic flow field (dashed lines). First considering the velocity distributions, it is evident how the two simulation models predict very similar flow configurations in a relatively complex flow field. Indeed, while in the converging region of the nozzle a common configuration is recognized, with a wide isentropic free-stream contoured by a narrow boundary-layer, in the diverging part the isentropic core rapidly vanishes and spanwise gradients affect the entire cross-section, leading to fully-developed profile. By looking at the two-dimensional velocity contours in Figure 8(a) sharp angle at the throat promotes a thickening of the boundary layer, whose dimension rapidly becomes comparable with the nozzle height in the diverging channel, as also confirmed by the spanwise velocity distributions before and after the throat in Figure 8(b).

Such flow field in the diverging part of the nozzle is mostly due to the very low aspect ratio of the duct, but also the very small scale of the experiment plays a role. The diverging duct is indeed so narrow that the

This is a preprint of the following article: Romei, A., & Persico, G., *Computational fluid-dynamic modelling of two-phase compressible flows of carbon dioxide in supercritical conditions*, Appl. Therm. Eng., 2021.
The published article may differ from this preprint, and is available at: 10.1016/j.applthermaleng.2021.116816

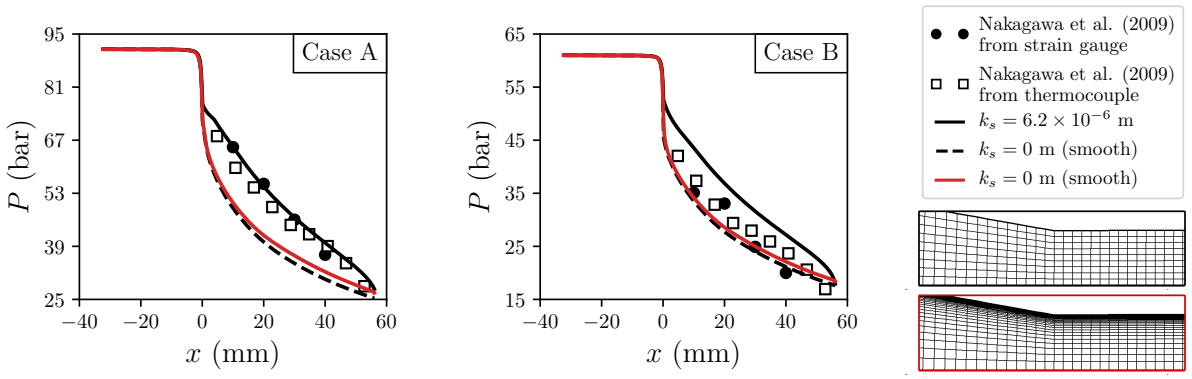

Figure 9: Impact of surface roughness on the flow solution for case A. Black lines correspond to results obtained with the rough-wall mesh (no wall resolution), while pressure distributions in red come from the mesh with a cell clustering at the wall ($y^+ < 1$). All these results are obtained with the mixture model.

wall roughness also significantly contributes to determine the flow configuration. In this work, the surface roughness adopted in [41] is considered, but two further comparative simulations for hydraulically smooth walls were performed. The first one employs the same wall resolution of the rough-wall simulations, and hence resorts to wall-functions for the near-wall treatment, while the second one features a refined mesh clustering at the wall so to achieve $y^+ < 1$ all over the wall boundaries. These two further simulations are compared to the one obtained with rough wall in Figure 9 for both case A and case B. The two smooth-wall simulations show only marginal differences on the pressure profiles (with a slight quantitative differences amplifying towards the nozzle outflow), but they exhibit a considerable difference with respect to the rough-wall simulation, highlighting the significance of the wall roughness in this experiment. Unfortunately, Nakagawa *et al.* did not provide any information about the actual roughness level; however, a level of roughness must be considered in the simulation as the wall cannot be considered hydraulically smooth given the small-scale nozzle. As a matter of fact, the roughness should be around two order of magnitude lower than the one employed in this work to have hydraulically smooth surfaces, which is not compatible with up-to-date manufacturing processes. In this regard, a smooth-wall simulation is just intended to represent an idealized case for the quantification of roughness effect and not an attempt to match experimental data. Indeed, the importance of the roughness is not only quantitative, but also qualitative. For smooth-wall simulations the flow regime is found to be supersonic in the diverging part, thus the expansion processes is driven by the converging-diverging shape of the nozzle. On the other hand, the rough-wall simulation does not predict a sonic Mach number at the throat, as it will be clearly shown in the last section of this manuscript, in which several two-phase speed-of-sound formulations are discussed. The pressure drop in the diverging part of the nozzle is then prompted by frictional losses, as originally argued by Nakagawa and his co-authors when discussing the experimental trends. From this angle, the better quantitative adherence of case B with

This is a preprint of the following article: Romei, A., & Persico, G., *Computational fluid-dynamic modelling of two-phase compressible flows of carbon dioxide in supercritical conditions*, Appl. Therm. Eng., 2021.
The published article may differ from this preprint, and is available at: 10.1016/j.applthermaleng.2021.116816

experimental data assuming a smooth wall is misleading. Furthermore, the rough-wall simulation better captures the overall pressure trend, notwithstanding the systematic overprediction. The reason of such overprediction for case B can be twofold: an uncertainty in the roughness level, although large deviations from the actual level is not expected in the light of present manufacturing processes, and meta-stable effects, which are more prominent far from the critical point.

The presence of the roughness also affects the mass-flow rate that passes through the nozzle, as reported in Table 3. For both upstream states, the mass flow rate increases of $10 - 15\%$ from rough- to smooth-wall simulations owing to a decrease of frictional losses. All cases were also simulated with the barotropic model: the higher discrepancy in the elaborated mass-flow rate is found for rough-wall simulation and amounts to $\sim 1.5\%$. As rough-wall simulations do not predict a sonic throat, the mass-flow rate is determined by the flow conditions at the nozzle outlet, in which the neglected effect of entropy on the density value is maximum. For smooth-wall simulations, the flow conditions at the throat establish the mass-flow rate. Given that the core is isentropic at the throat, the only differences between the two models regard the spanwise density distribution and small discrepancies in the computed velocity field ($\sim 0.5\%$). Finally, in smooth-wall simulations the barotropic model overestimates both expansion processes compared to the mixture model, with an outlet pressure which is around 7% lower than the mixture-model counterpart. The larger discrepancy depends on the role of the density in determining the expansion process: in smooth-wall simulation, a supersonic expansion takes place in the diverging portion of the nozzle. The density predicted by the barotropic model does not consider the influence of the entropy that still raises along the axis, notwithstanding the smooth-wall assumption, hence the density is smaller than the one predicted by the thermodynamically complete mixture model. As a consequence, the flow expands more in the diverging duct, explaining the larger deviations. In rough-wall simulations, on the other hand, the expansion is dictated by frictional losses, therefore the volumetric evolution plays a minor role. It is to be noted that, for adiabatic flows, the barotropic model could be easily improved by resorting to non-isentropic laws for the variability of thermo-physical properties along the transformation. In practice, a preliminary barotropic simulation can be performed using isentropic laws, then the resulting entropy raise can be estimated with the procedure reported above and the barotropic relationships updated to incorporate the effect of the entropy rise (as done, for example, when computing the polytropic efficiency in turbomachinery analysis). Then, a new barotropic simulation, implementing the so-estimated non-isentropic relationships, can be performed to better approximate the actual density change. Figure 8(b) indicates that one iteration should be sufficient to estimate accurately the impact of entropy rise on the density.

All quantitative comparisons are reported in Appendix A: Table A.6 reports the maximum and minimum deviation of the barotropic model from the mixture model, while the local pressure and temperature values at measurement locations alongside the experimental data are reported in Table A.7.

The flow configuration is complex not only on the aerodynamic ground, but also introduces thermody-

This is a preprint of the following article: Romei, A., & Persico, G., *Computational fluid-dynamic modelling of two-phase compressible flows of carbon dioxide in supercritical conditions*, Appl. Therm. Eng., 2021.
The published article may differ from this preprint, and is available at: 10.1016/j.applthermaleng.2021.116816

Table 3: Comparison of the mass-flow rate predicted by the mixture and the barotropic model for all simulated cavitating flows.

	Wall functions	$\dot{m}_{mix}$ (kg/s)	$\dot{m}_{baro}$ (kg/s)	$\varepsilon_{mix-baro}$ (%)
		Case A		
Rough wall	✓	4.72	4.80	−1.54
Smooth wall	✓	5.43	5.40	0.59
Smooth wall		5.39	5.36	0.45
		Case B		
Rough wall	✓	3.71	3.77	−1.60
Smooth wall	✓	4.19	4.20	−0.67
Smooth wall		4.16	4.17	−0.33

namic challenges, resulting a very critical benchmark for the present barotropic model, which was constructed by assuming an isentropic pressure-density relation. However, the velocity field reproduced by the barotropic model is aligned with the mixture one (maximum deviations in the range of 0.5%), also in the region of developed profiles, where entropy is generated in the boundary layer. Moreover, by inspecting the entropy generation along the nozzle axis, it is evident that the barotropic flow solution, once properly post-processed, can be used to achieve realistic estimates of the mechanical dissipation processes, regardless of the isentropic pressure-density relationship adopted. As a result, when the estimated entropy and the computed pressure are combined to obtain the generation of vapour mass fraction along the nozzle, a remarkable agreement is found between the barotropic model and the complete mixture model, in terms of transition onset, overall trend, and quantitative levels, as visible in Figure 7.

Due to the fully developed profiles observed in the diverging region of the nozzle, the distributions in cross-stream direction are expected to be highly non-uniform for all the quantities, including the vapour mass fraction. The spanwise distributions of w_V at three different axial locations are reported in Figure 10 for case A, showing a consistent increase close to the wall. This can be explained by considering that higher entropy level is found moving away from the nozzle axis, due to the dissipation in the boundary layer. The rise of entropy further increases the vapour quality with respect to that of the flow in the nozzle axis (which is, in turn, higher with respect to the ideal quality in presence of an isentropic expansion). As a result, the vapour-mass fraction at the wall is $3 - 5\%$ higher than the free-stream value. In these trends, slight but visible differences appear between the results obtained with the mixture model and with the barotropic one. This is a consequence of the uniform total enthalpy assumption in the post-processing of the barotropic

This is a preprint of the following article: Romei, A., & Persico, G., *Computational fluid-dynamic modelling of two-phase compressible flows of carbon dioxide in supercritical conditions*, Appl. Therm. Eng., 2021.
The published article may differ from this preprint, and is available at: 10.1016/j.applthermaleng.2021.116816

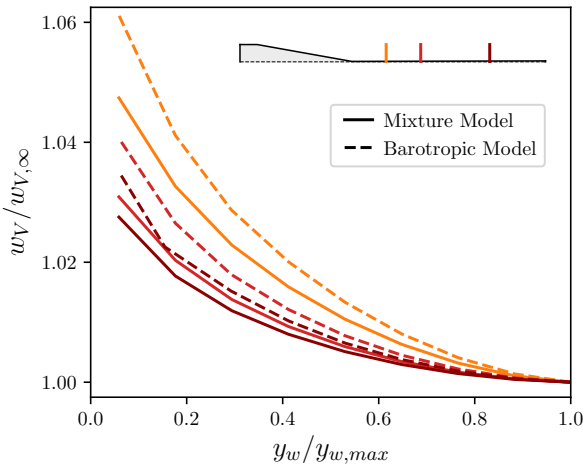

Figure 10: Vapour-mass fraction of case A normalised to the free-stream value at different axial locations, namely at $x = 10\,\text{mm}$ (orange lines), 20 mm (red lines) and 40 mm (dark-red lines).

solution: close to the wall, the fluid heated by dissipation exchanges heat with the fluid away from the wall, resulting in a slight reduction of the total enthalpy. This effect, as already noted, cannot be captured in the processing of the barotropic flow solution, which eventually results in a slight overestimate of the enthalpy close to the wall. Consequently, the mass fraction of vapour is slightly overestimated in barotropic estimation, although the discrepancy remains within 1% of the local nozzle-axis value.

The good accuracy of the barotropic flow solution is worth for further physical investigations. As already remarked, the barotropic model implies to consider the fluid compressible but not thermally expandable, i.e. to assume the thermal expansion coefficient $\beta = -\frac{1}{\rho}\left(\frac{\partial \rho}{\partial T}\right)_P$ equal to zero. Figure 11 reports the distribution β for the carbon dioxide in single-phase above saturation, including the liquid, the supercritical and the superheated vapour region. To highlight the effects of thermal expansion, logarithmic scale is used for the contours. The plot indicates that the carbon dioxide is prone to thermal expansion only in a narrow region adjacent to the critical point, where the fluid exhibits severe gradients in all the thermo-physical properties. Among the thermo-physical properties of interest, in the critical region the isobaric heat capacity c_P grows significantly (becoming theoretically infinite at the critical point) , as illustrated by the black dashed isolines superposed in the figure. The combination of high β and high c_P in the critical region is a further indication of the technical relevance of the barotropic model: where thermal expansion is quantitatively significant, the amount of heat required to alter the fluid temperature is enormous and arguably not comparable with the heating due to viscous dissipation occurring in adiabatic flows.

The present theoretical interpretation indicates that the effects of the thermal expansion are limited for any of the cases investigated in this work, which are rather representative of technical applications such as compressors for sCO_2 power cycles. Therefore, if the above deviations between the simplified barotropic

This is a preprint of the following article: Romei, A., & Persico, G., *Computational fluid-dynamic modelling of two-phase compressible flows of carbon dioxide in supercritical conditions*, Appl. Therm. Eng., 2021.
The published article may differ from this preprint, and is available at: 10.1016/j.applthermaleng.2021.116816

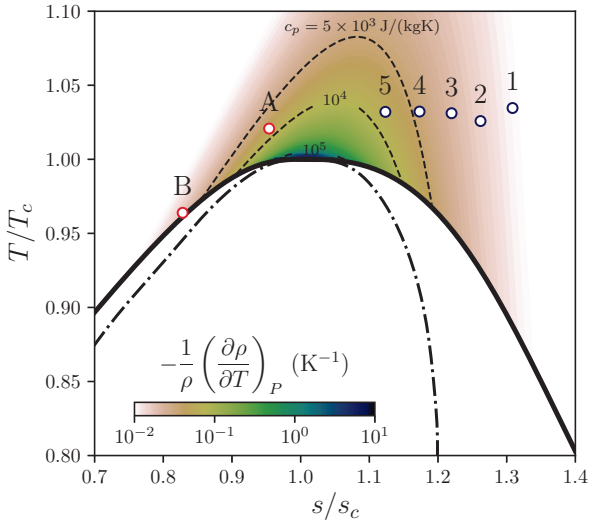

Figure 11: Volumetric coefficient of thermal expansion and isobaric specific heat (black dashed lines) for single-phase CO_2.

modeling and the thermodynamically complete mixture model are acceptable, the barotropic model would be recommended in the light of its computational robustness and efficiency.

4.2. Condensing flows

In condensing flows the primary phase is the vapour phase $\alpha_p = \alpha_V$, while the secondary phase is the liquid phase $\alpha_d = \alpha_L$. The phase change is activated when $P > P_{sat}(T)$.

The computational procedure resembles the one previously described for the cavitating case. Total pressure and total temperature are prescribed at the inlet section as in Table 1 for the five flow configurations, imposing $\alpha_L = 0$ therein (the flow enters only in vapour phase). For the barotropic model, only the total pressure is specified. To impose the typical low turbulence level of a flow expanding from a reservoir, a hydraulic diameter equal to 12.6 mm, i.e. twice the height of the inlet section, and an eddy viscosity ratio equal to 2.5 are assigned as turbulent boundary conditions. As the flow regime is always supersonic, the solver ignores the static pressure value imposed at the outlet. No-slip and adiabatic boundary conditions are prescribed at the wall, while a symmetry condition is imposed at the nozzle axis. Differently from the cavitation experiment, the nozzle used for the condensation study is of sufficiently large scale that the wall is modelled as smooth (the nozzle throat is one order of magnitude larger than that of the previous nozzle). Moreover, as a supersonic expansion always takes place in the diverging section, the effect of roughness is expected to be secondary in determining the flow evolution. The numerical schemes and the solver strategy are identical to the ones already introduced in §4.1. The penalty constant is set to $\mathcal{K} = 10^3$ as in the previous section. It is anticipated that the resulting constraint violation $P - P_{sat}(T)$ is limited to $\sim 1\%$ in the neighbourhood of the phase-change onset, reducing of one order of magnitude in the ongoing expansion.

This is a preprint of the following article: Romei, A., & Persico, G., *Computational fluid-dynamic modelling of two-phase compressible flows of carbon dioxide in supercritical conditions*, Appl. Therm. Eng., 2021.
The published article may differ from this preprint, and is available at: 10.1016/j.applthermaleng.2021.116816

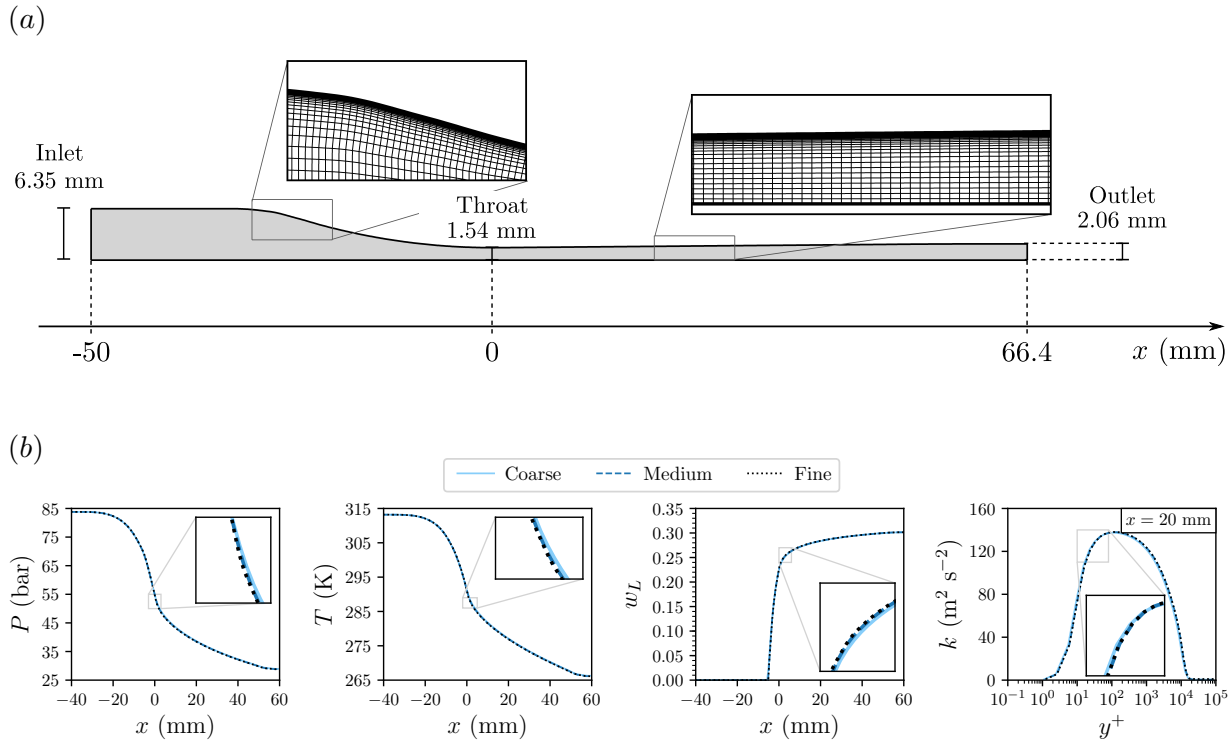

Figure 12: Grid-convergence assessment for condensing-flow simulations: (a) the medium mesh is selected as the grid-independent mesh (number of elements $\approx 5 \times 10^4$, grid resolution at the throat $\approx 2 \times 10^{-4}$ m, 20 cells in the boundary layer with a first-layer wall distance of 3×10^{-8} m) alongside the main nozzle dimensions, (b) pressure, temperature, liquid-mass fraction and turbulent kinetic energy distributions for different grid refinements. The grid-convergence study is performed on case 5.

A grid convergence assessment was carried out by generating three structured meshes with an increasing number of elements. The number of elements was doubled each time in both x- and y-directions while keeping the same wall resolution. Coherently with the smooth-wall condition in combination to the $k-\omega$ SST turbulence model, the near-wall region of the mesh was constructed to avoid the use of wall functions and it is composed by 20 layers in the boundary layer, with a first-layer wall distance equal to 3×10^{-8} m. The maximum $y^+ = 1.2$ is found for the case 5 with three cells within the viscous sub-layer ($y^+ < 10$). The flow model used in this grid study is the mixture model and we focus on the expansion process closer to the thermodynamic critical point (case 5). Pressure, temperature and liquid-mass fraction trends along the nozzle axis are reported in Figure 12(b) alongside the turbulent kinetic energy distribution at a specified axial location ($x = 20$ mm). This latter quantity is reported in a logarithmic scale as a function of the dimensionless wall distance to better highlight the trend of the turbulent kinetic energy close to the wall. As in the previous section, the geometrical discretization error is quantified by computing the GCI between the medium and the fine mesh of pressure, temperature and liquid mass fraction at the throat and at different

This is a preprint of the following article: Romei, A., & Persico, G., *Computational fluid-dynamic modelling of two-phase compressible flows of carbon dioxide in supercritical conditions*, Appl. Therm. Eng., 2021.
The published article may differ from this preprint, and is available at: 10.1016/j.applthermaleng.2021.116816

Table 4: Grid convergence indexes for pressure, temperature and liquid-mass fraction at selected axial locations along the diverging section. The grid-convergence study is performed on case 5.

	GCI		
x (mm)	P (%)	T (%)	w_L (%)
0	0.67	0.12	−2.53
15	0.03	0.00	−0.01
30	0.02	0.00	−0.01
45	0.01	0.00	0.00
60	0.00	0.00	0.00

axial location along the diverging portion. The highest values are found at the throat location where the gradients are larger. In particular, the GCI for the liquid mass fraction is 2.53% as a consequence of the steep increase of the dispersed phase at the throat, see Figure 12(b). Since the flow is supersonic, the mass-flow rate is determined by the flow conditions at the throat; however, the GCI for the mass flow rate is 0.02%. Such low value combined with GCIs smaller than 0.03% throughout the divergent testifies the adequacy of the medium mesh. Therefore, the medium mesh is selected for all the following analyses: it contains $\approx 5 \times 10^4$ hexahedral elements with a grid resolution at the throat of 2×10^{-4} m. Within the free-stream region, the aspect ratio is around 1.5 in the convergent, which raises up to 2.5 at the throat, then reducing to 2.0 in the divergent.

Figure 13 reports the comparison of pressure and the liquid-mass fraction distributions against experimental data for the five condensing flows. The differences in the distributions along the nozzle axis between the mixture and the barotropic do not exceed 1%. As the boundary layers remain confined in a narrow region close to the wall along the entire nozzle length, the barotropic model constructed using an isentropic pressure-density relationship provides an exact description of the thermodynamics of the fluid expansion in the core region of the nozzle, both in the single-phase and in the two-phase region - in the limit of a HEM two-phase flow representation. A further proof is provided by the excellent agreement (within 0.1%) of the mass-flow rate predicted by the two models, as reported in Table 5. As the flow is supersonic, the mass-flow rate depends on the flow conditions at the throat. Depending on the specific case, the two-phase flow can already be established at the throat, confirming the quality of the barotropic modeling in also representing the two-phase flow.

When comparing the numerical results to the experiments in Figure 13, the larger pressure discrepancy is found right after the onset of the phase change, where the experimental data exhibit a sudden change in the pressure trend. Furthermore, for the first two cases, an unconventional knee is noticed in the pressure

This is a preprint of the following article: Romei, A., & Persico, G., *Computational fluid-dynamic modelling of two-phase compressible flows of carbon dioxide in supercritical conditions*, Appl. Therm. Eng., 2021.
The published article may differ from this preprint, and is available at: 10.1016/j.applthermaleng.2021.116816

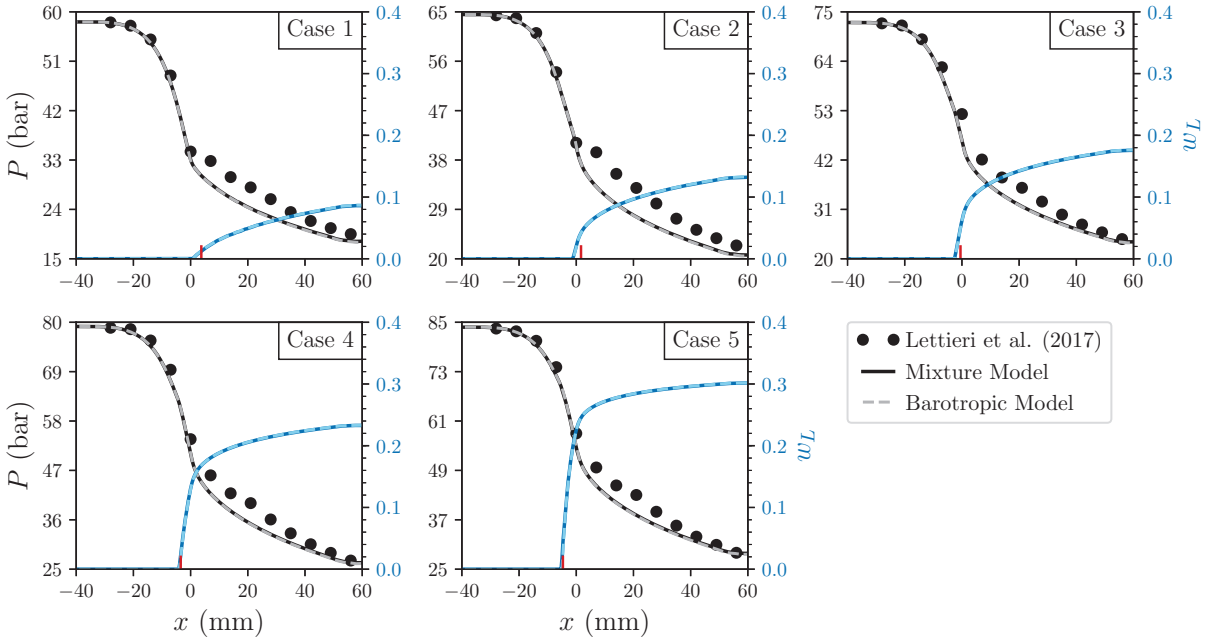

Figure 13: Comparison of the mixture (solid lines) and barotropic (dashed lines) model against experimental data along the nozzle axis. The red tick identifies the condensation onset observed experimentally by Lettieri *et al.* [9, Tab. 3]. The liquid-mass fraction predicted by the barotropic model is computed as a post-processing.

Table 5: Comparison of the mass-flow rate predicted by the mixture and the barotropic model for all simulated condensing flows.

	$\dot{m}_{mix}$ (kg/s)	$\dot{m}_{baro}$ (kg/s)	$\varepsilon_{mix-baro}$ (%)
Case 1	29.43	29.46	−0.08
Case 2	33.64	33.66	−0.06
Case 3	38.97	38.99	−0.04
Case 4	44.02	44.04	−0.03
Case 5	48.94	48.95	−0.02

trend close the phase-transition onset, producing a concavity in the pressure trend which remains negative in the first part of the divergent. This feature is not captured by the models, which instead predict a more conventional pressure trend, which smoothly evolves from a negative concavity in the convergent to a positive concavity in the divergent. Such a peculiar trend in the experimental data probably originates from meta-stable equilibrium states, which are expected to be prominent far from the critical point, delaying the phase transition. Lettieri *et al.* [9] actually identified meta-stability effects in their results, and even derived

This is a preprint of the following article: Romei, A., & Persico, G., *Computational fluid-dynamic modelling of two-phase compressible flows of carbon dioxide in supercritical conditions*, Appl. Therm. Eng., 2021.
The published article may differ from this preprint, and is available at: 10.1016/j.applthermaleng.2021.116816

experimental samples of the Wilson line. They actually found that the largest departure from conventional saturation applies for cases 1 and 2 of the present study , consistently with the largest discrepancy found in the present study, corresponding to 16% for cases 2. Apart from the peculiar trend in correspondence of the phase-transition onset, the overall pressure distribution is still properly captured by the model. The global deviation in according to the error defined in Eq. 11 is quantified as 5.7% and 6.4% for cases 1 and 2, respectively.

The agreement between experiments and simulations improves as long as the upstream total state gets closer to the thermodynamic critical point. For these cases, the meta-stability effects are reduced, although they are still present as reported in the experimental reference. An obvious development of this work would be to include meta-stable states in the mixture model formulation, e.g. in a DEM fashion, notwithstanding the cases of most interest for sCO_2 compressors are those in the proximity of the critical point (cases 4 and 5), for which deviations less than 10% are observed with respect to most of the experimental data. The overall trend is generally well captured, with a WMAPE of 4.5% and 4.1% for cases 4 and 5, respectively. All local deviations with respect to the available measurements are quantified in Table A.8.

Despite the meta-stability effects discussed above, it is worth highlighting that the present simulation model predicts the condensation onset in a very good approximation for all the cases. In the experiment, the position of transition onset was derived from optical measurement, and it is reported in the frames of Figure 13 as a red tick. In fact, a slight discrepancy is found for the cases far from the critical point (Cases 1 and 2), while a perfect matching is achieved for the expansions from the supercritical state (Cases 4 and 5). This is fully consistent with the above meta-stability effects, but we also note that the experimental identification of condensation point may be affected by a larger uncertainty for Cases 1, 2 and 3. In such cases, the transition is smoother and it is not straightforward to exactly identify the axial location at which the phase change starts, see [9, Fig. 9]. The opposite occurs for the near-critical cases 4 and 5, for that the identification is made easier by the rapid growth of the condensed mass fraction, and the matching with the experiment becomes excellent.

The corresponding mass-fraction flow fields computed by the mixture models are reported in Fig. 14. The flow fields are qualitatively similar to the experimental visualization made by Lettieri *et al.*, in which the condensation location moves back in the nozzle while the upstream thermodynamic state gets closer to the critical point.

5. Mixture speed-of-sound formulation

The two computational models introduced in this work have been shown to reproduce, with a good or acceptable accuracy, the experimental results of compressible two-phase flows, both for cavitation and condensation. Since both models are built on the two-fluid concept, which describes the mixture evolution

This is a preprint of the following article: Romei, A., & Persico, G., *Computational fluid-dynamic modelling of two-phase compressible flows of carbon dioxide in supercritical conditions*, Appl. Therm. Eng., 2021.
The published article may differ from this preprint, and is available at: 10.1016/j.applthermaleng.2021.116816

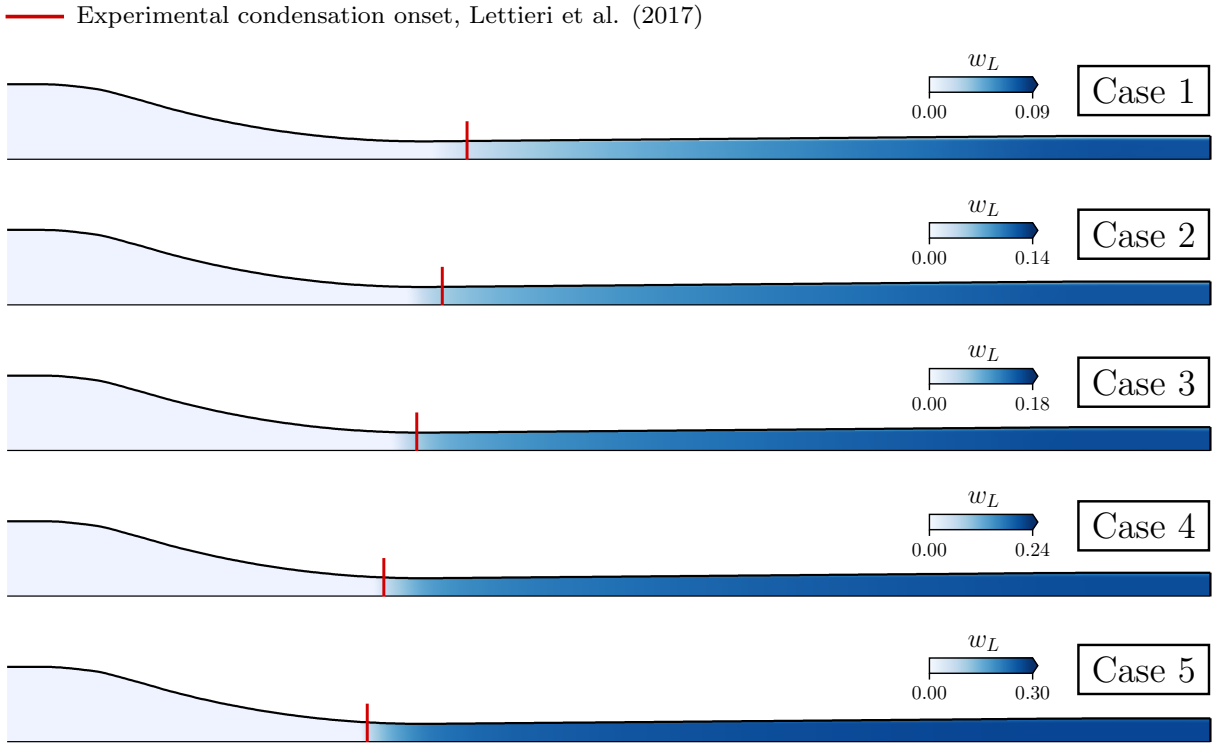

Figure 14: Liquid-mass fraction distributions for the five condensing flows as predicted by the mixture model. The red tick identifies the condensation onset observed experimentally by Lettieri *et al.* [9, Tab. 3]

without detailing the local interfaces between phases, the concept of speed of sound can be extended to the mixture and a 'surrogate' expression for that can be defined.

The definition of the mixture speed of sound is closely linked to the employed two-phase models and its associated assumptions [21, 39]. Moreover, it was demonstrated that the more the system is constrained, the lower the corresponding speed of sound [44, 45]. It means that the HEM speed of sound will be lower than the speed of sound of a HFM, which relaxes the thermal equilibrium assumption. Specifically, the HEM speed of sound is expressed as:

$$c_m^2 = \left(\frac{\partial P}{\partial \rho_m}\right)_s \tag{12}$$

Given the assumptions of the mixture and barotropic model, we expect that this relationship should be used in the determination of the speed of sound and to assess whether or not the flow regime is supersonic. By default, Ansys-Fluent® makes use of the speed-of-sound formulation originally conceived by Wood [46]:

$$\frac{1}{\rho_m c_m^2} = \frac{\alpha_L}{\rho_L c_L^2} + \frac{\alpha_V}{\rho_V c_V^2} \tag{13}$$

The expression says that the bulk modulus of the mixture $\rho_m c_m^2$ is the harmonic average of the bulk

This is a preprint of the following article: Romei, A., & Persico, G., *Computational fluid-dynamic modelling of two-phase compressible flows of carbon dioxide in supercritical conditions*, Appl. Therm. Eng., 2021.
The published article may differ from this preprint, and is available at: 10.1016/j.applthermaleng.2021.116816

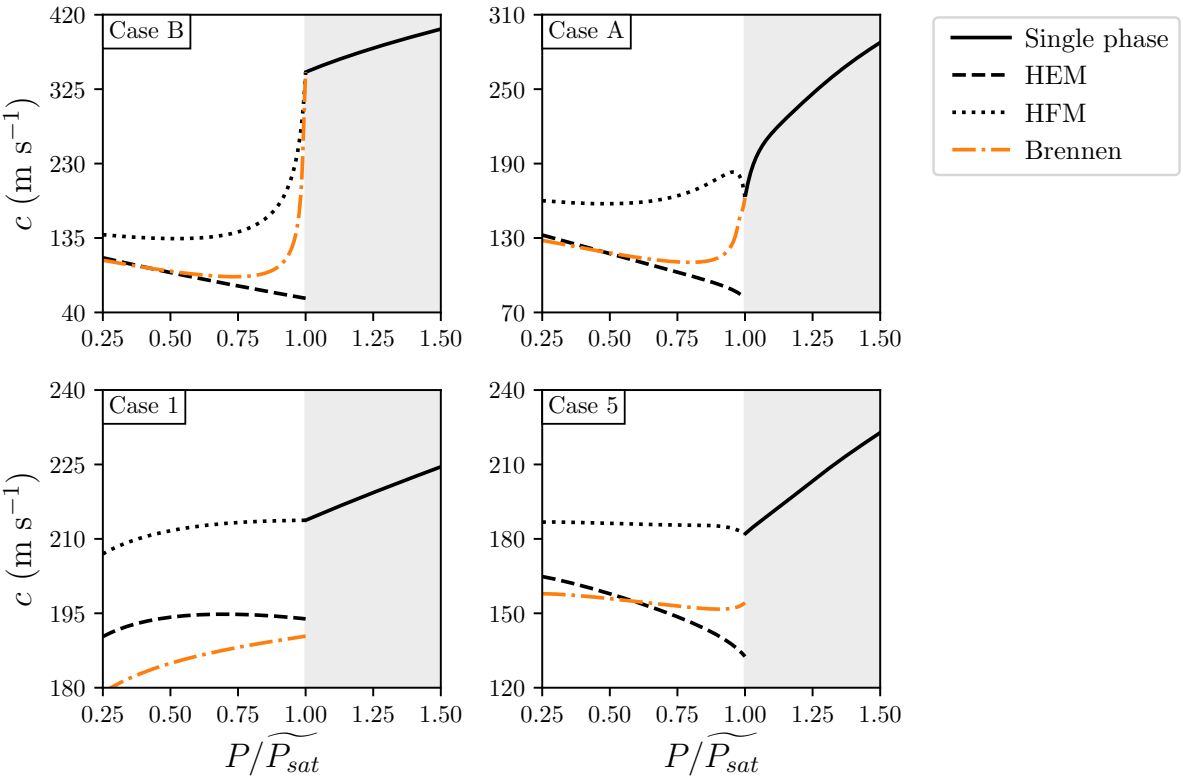

Figure 15: Comparison among different two-phase speed-of-sound formulations: homogeneous equilibrium model (Equation 12), homogeneous frozen model (Equation 13) and an hybrid formulation between the homogeneous equilibrium model and the homogeneous frozen model proposed by Brennen [19] (Equation 15).

moduli of the components weighted on their volume fractions. Such definition is derived on the basis of the single-phase volumetric behaviours, hence it excludes any thermal effects between them. For this reason, it can be used under HFM assumptions and it is widely used in presence of multi-component flows which do not chemically react. In analogy with the analysis of Giacomelli *et al.* [25], we also include the definition of the mixture speed of sound provided by Brennen [19].

$$\frac{1}{\rho_m c_m^2} = \frac{\alpha_V}{P}[(1-\epsilon_V)f_V + \epsilon_V g_V] + \frac{\alpha_L}{P}[(1-\epsilon_L)f_L + \epsilon_L g_L] \tag{14}$$

which considers that a portion of the phases can exchange heat and momentum instantaneously (ϵ_L, ϵ_V), promoting equilibrium, and the remaining portion ($1-\epsilon_L$, $1-\epsilon_V$) does not contribute to the exchange, promoting disequilibrium. In this way, depending on the portion of fluid involved in the phase change, either the HEM ($\epsilon_L = \epsilon_V = 1$) or the HFM ($\epsilon_L = \epsilon_V = 0$) can be recovered. On top of that, Brennen suggested the following approximations: $f_V = g_V \approx 1$, $f_L \approx 0$, $\epsilon_L \approx \alpha_V$, and $g_L \approx 2.1(P/P_c)^{-0.566}$ for carbon dioxide only. Plugging into Eq. (14) the above simplifications, the following expression for the mixture speed of

This is a preprint of the following article: Romei, A., & Persico, G., *Computational fluid-dynamic modelling of two-phase compressible flows of carbon dioxide in supercritical conditions*, Appl. Therm. Eng., 2021.
The published article may differ from this preprint, and is available at: 10.1016/j.applthermaleng.2021.116816

sound is obtained:

$$\frac{1}{\rho_m c_m^2} = 2.1 \frac{\alpha_L \alpha_V}{P^{1.566}} P_c^{0.566} + \frac{\alpha_V}{P} \tag{15}$$

Figure 15 reports the speeds of sound computed according to three expressions (12), (13) and (15) for isentropic expansions of cavitating (case A and B) and condensing (case 1 and 5) flows. The HEM speed of sound exhibits a discontinuity at the saturation [44], which is more pronounced for cavitating flows. Interestingly, the HEM speed of sound generally increases along isentropic expansion (unless case 1, which is far from the critical point and applications of interest) while the single-phase carbon-dioxide speed of sound always decreases along isentropic expansion. Such evidence can be interpreted in terms of the fundamental derivative of the gas dynamics $\Gamma = 1 + \frac{\rho}{c}\left(\frac{\partial c}{\partial \rho}\right)_s$ [47], which is lower than the unity in the two-phase region of carbon dioxide. Moreover, under the HEM assumptions, $\Gamma < 0$ in the near-critical two-phase region [48], paving the way for the occurrence of non-classical effects [49]. The HFM expression constantly overpredicts the speed of sound compared to the HEM predictions in accordance with the above explanation related to the equilibrium assumptions and associated speed-of-sound values. Regarding Brennen's expressions, as the simplified derivation was conceived between HEM and HFM, the speed of sound should be contained among the corresponding HEM and HFM values. When looking at cavitating cases, Brennen's formulation does exactly what it is meant to be. Right after the phase transition, the disequilibrium between phases is expected to be maximum and for this reason the speed-of-sound value is larger than the corresponding HEM value. However, as long as the expansion process proceeds, the two expressions collapse in a good approximation. It is worth specifying that the expression (15) shows a spike for cavitating flows at the saturation, possibly due to the approximations that were introduced. To avoid this unphysical behaviour, the maximum speed of sound was limited at the single-phase speed of sound. On the other hand, when Brennen's formulation is applied to condensing flows, unphysical trends are obtained: in case 1, Brennen's speed of sound is lower than the corresponding HEM value, which is not admissible as the HEM should be the lowest among all speed-of-sound formulations. Approaching the critical point, as in case 5, it seems to recover the correct trend (similar to cavitating flows), but as long as the expansion proceeds, Brennen's expression tends to underestimate the HEM value with a non-negligible error. Finally, it is noted that the discontinuity in the speed of sound predicted by the HEM formulation is generally smaller in condensing flows than cavitating flows, as reported in Figure 15 for exemplary upstream conditions. From this analysis, we conclude that the expression provided by Brennen can be effectively used in modelling cavitating flows, while it is not adequate for condensing flows of carbon dioxide.

The three speed-of-sound formulations are then applied in the post-process of case A (cavitation) and case 5 (condensation), which are the cases closest to the critical point among those presented in this work for the two categories of phase transition. Analogous studies involving the HFM and Brennen's formulation

This is a preprint of the following article: Romei, A., & Persico, G., *Computational fluid-dynamic modelling of two-phase compressible flows of carbon dioxide in supercritical conditions*, Appl. Therm. Eng., 2021.
The published article may differ from this preprint, and is available at: 10.1016/j.applthermaleng.2021.116816

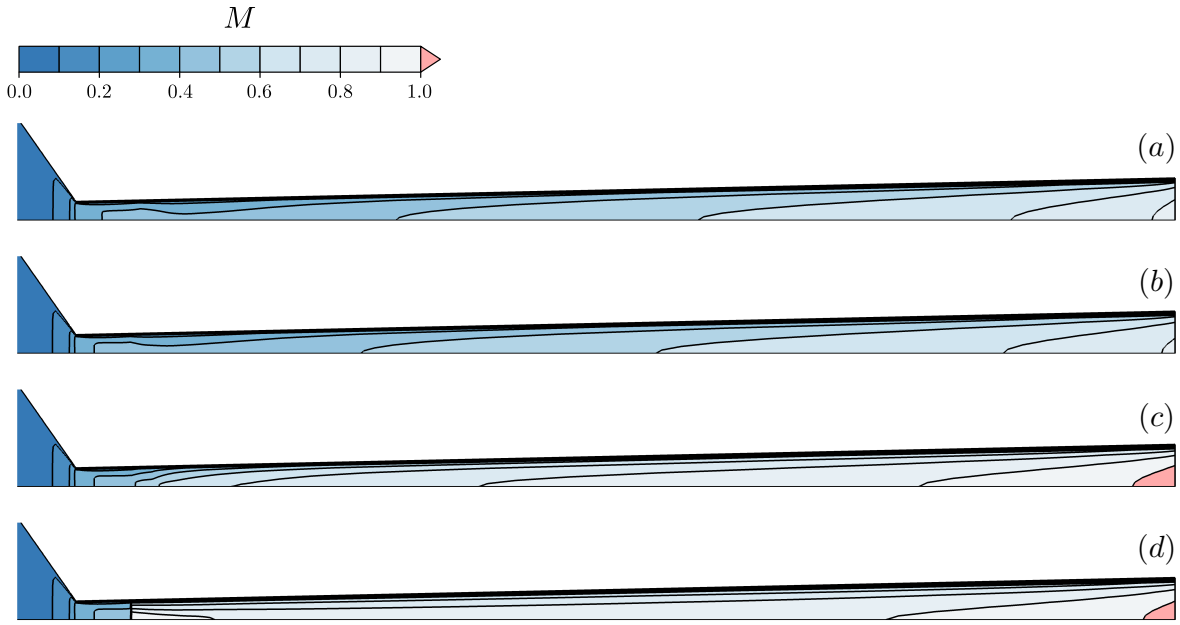

Figure 16: Mach number distributions for the case A (cavitating flow) using different two-phase speed-of-sound formulation: (*a*) Ansys-Fluent® mixture-model built-in formulation, (*b*) HFM, (*c*) Brennen, (*d*) HEM. For visualization purposes, the x-direction is stretched such that $x/y = 0.125$ and the convergent section is not shown.

are reported in [50, 25] for cavitating flows. To the authors' knowledge, similar studies for condensing flows are not available.

Figure 16 displays the Mach number fields for case A (cavitation). Specifically, Figure 16(*a*) is the Mach number field as provided by Ansys-Fluent® for the mixture model, while Figures 16(*b*–*d*) are obtained by setting the three different speed-of-sound formulations in the equation (10) of the barotropic model. First, the nearly identical distributions obtained in Figure 16(*a*)–(*b*) confirms that the present version of Ansys-Fluent® makes use of equation (13) as a post-processing for the mixture speed of sound. As a consequence of the higher speed of sound under HFM assumptions, the Mach number is everywhere lower than unity, reaching the maximum value of $M = 0.82$ at the nozzle outlet. In accordance with Figure 15, the main difference between Figure 16(*c*)–(*d*) is located at the phase-transition onset, in which the HEM model predicts a sudden drop. Brennen's formulation instead smears the discontinuity, then recovering approximately the same Mach number evolution predicted by the HEM formulation towards the nozzle outlet, in which a slightly supersonic Mach number ($M = 1.06$) is predicted.

As a final comment, the Mach number field obtained with Brennen's model, which accepts a degree of disequilibrium, do not diverge significantly from solutions obtained with HEM simulation tools. This finding provides a crucial indication on the technical relevance of CFD simulations tools based on the assumption

This is a preprint of the following article: Romei, A., & Persico, G., *Computational fluid-dynamic modelling of two-phase compressible flows of carbon dioxide in supercritical conditions*, Appl. Therm. Eng., 2021.
The published article may differ from this preprint, and is available at: 10.1016/j.applthermaleng.2021.116816

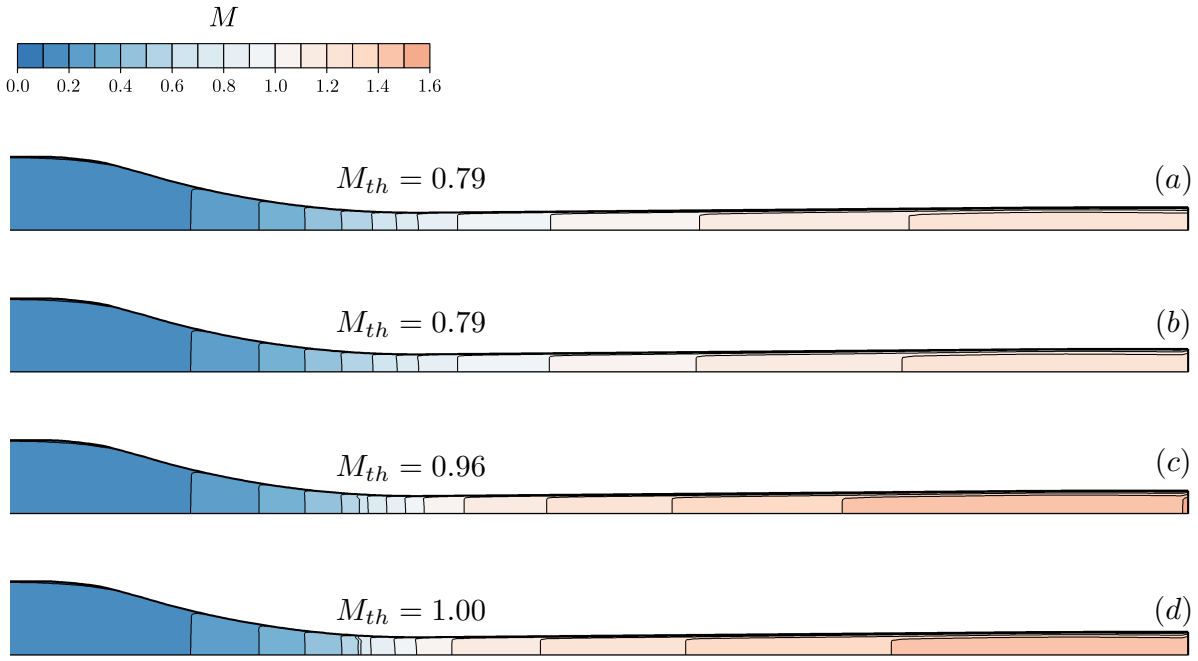

Figure 17: Mach number distributions for the case 5 (condensing flow) using different two-phase speed-of-sound formulation: (*a*) Ansys-Fluent® mixture-model built-in formulation, (*b*) HFM, (*c*) Brennen, (*d*) HEM. The Mach number at the geometrical throat M_{th} is also reported.

of homogeneous equilibrium for sCO_2 compressor design and analysis, especially when it comes to the identification of the choking limit.

A similar analysis is illustrated in Figure 17 for the case 5 (condensation). Again, the default choice of Ansys-Fluent® , which corresponds to the HFM formulation, provides the lowest Mach number, with the onset of the sonic Mach number after the geometrical throat. Although the sonic throat may be different from the geometrical one when the boundary layer is considered, the streamwise location where the sonic Mach number onsets seems not consistent with the boundary-layer displacement thickness. This observation corroborates the idea that the expression for the speed of sound in (13) is not consistent with the HEM governing equations. On the other hand, the HEM expression (12) predicts a sonic Mach number in the geometrical throat, consistently with the assumptions of the model. As a matter of fact, in presence of mechanical and thermal equilibrium among phases, the single-phase gas dynamics should be theoretically recovered for the mixture. Finally, although the supersonic expansion in the divergent, with an outlet Mach number larger than the HEM counterpart, Brennen's model does not predict a sonic Mach number at the throat; as already mentioned, the corresponding speed of sound exhibits an unphysical trend when applied to condensing flows.

This is a preprint of the following article: Romei, A., & Persico, G., *Computational fluid-dynamic modelling of two-phase compressible flows of carbon dioxide in supercritical conditions*, Appl. Therm. Eng., 2021.
The published article may differ from this preprint, and is available at: 10.1016/j.applthermaleng.2021.116816

6. Conclusion

The paper has presented and discussed two computational strategies to simulate compressible two-phase flows of carbon dioxide for industrial applications, operating in the proximity of the thermodynamic critical point and in supercritical conditions. Both models rely on the description of the mixture properties by resorting to the so-called two-fluid concept, thus eliminating the need of detailing the local interaction between phases. This allows to achieve a considerable simplification in the mathematical modeling, in view of their application to the design and analysis of supercritical carbon dioxide compressors. The first formulation, named *mixture model*, consists in the full-set of governing equations for the mixture plus an additional transport equation that governs the phase transitions; the onset of phase change is driven by the difference between the local pressure and the saturation pressure at the local temperature, by resorting to a penalty formulation. The second formulation, named *barotropic model*, strictly assumes mechanical and thermal equilibrium and the mixture thermo-physical properties are expressed as functions of the pressure only. These simplifications leads to a reduction of the overall computational cost alongside an increased solver robustness, by virtue of the simplified thermodynamic treatment.

The two models have been compared against experiments published in literature for cavitating (liquid $\mapsto$ vapour) and condensing (vapour $\mapsto$ liquid) flows. Both the comparisons involve expansion processes that progressively approach the critical point, where large discrepancies from the ideal-gas thermodynamics are observed. The two models exhibit a remarkable agreement with each other and are able to reproduce the trends set by the experimental data, also showing an overall good quantitative agreement with measured data. For the expansions evolving from supercritical states, the weighted mean absolute percentage error of pressure evaluated along the whole expansions resulted of about 2% and 4% for cavitating and condensing flow respectively; in case of supercritical cavitating flows, for that also temperature measurements are available, the same global error in terms of temperature resulted below 1%.

More significant quantitative differences emerge when considering expansions evolving from subcritical states. We conjecture that most of the deviations can be attributed to meta-stable effects, which might delay the phase-change onset in the conditions farthest from the critical point, or to the presence of a relative motion between phases. The mixture model, even though expressed under mechanical and thermal equilibrium in this work, is enough flexible to possibly relax these assumptions via constitutive equations, when detailed experimental data will enable their formulations for compressible flows of carbon dioxide. In the limit of the homogeneous equilibrium approximation, the barotropic model has been shown to provide comparable predictions of the expansion processes at a lower computational cost and with an improved solver robustness.

This is a preprint of the following article: Romei, A., & Persico, G., *Computational fluid-dynamic modelling of two-phase compressible flows of carbon dioxide in supercritical conditions*, Appl. Therm. Eng., 2021.
The published article may differ from this preprint, and is available at: 10.1016/j.applthermaleng.2021.116816

Appendix A. Tabular results

Experimental results for cavitating flows (case A and case B) were only reported by Nakagawa *et al.* [31] in a graphical form, hence the exact measurement locations as well as the associated values are not precisely known. Therefore, the following numerical comparisons have to account for this degree of approximation. The deviations between experimental and numerical values are computed as $\varepsilon = (X_{mix} - X_{exp})/X_{exp}$, where X can be either pressure or temperature. The smooth-wall results for cavitating flows refer to the one obtained with the refined mesh at the wall ($y^+ < 1$).

Table A.6: Maximum deviations in pressure predictions along the nozzle axis between mixture and barotropic model.

$\frac{P_{mix} - P_{baro}}{P_{mix}}$	**Case A** Rough	**Case A** Smooth	**Case B** Rough	**Case B** Smooth	**Case 1**	**Case 2**	**Case 3**	**Case 4**	**Case 5**
Max	2.9%	7.4%	2.3%	7.2%	1.0%	0.9%	0.9%	0.8%	0.9%
Min	0.0%	−0.1%	0.0%	0.0%	0.0%	−0.6%	−0.3%	−0.3%	−0.5%

Table A.7: Comparison of numerical predictions against experiments [31] for cavitating expansions.

	Case A						**Case B**					
	Rough			**Smooth**			**Rough**			**Smooth**		
x (mm)	P_{exp} (bar)	P_{mix} (bar)	ε (%)	P_{exp} (bar)	P_{mix} (bar)	ε (%)	P_{exp} (bar)	P_{mix} (bar)	ε (%)	P_{exp} (bar)	P_{mix} (bar)	ε (%)
10	65.17	65.18	0.0	65.17	50.51	−22.5	35.10	43.54	24.0	35.10	34.17	−2.6
20	55.47	54.70	−1.4	55.47	41.90	−24.5	33.06	36.87	11.5	33.06	28.58	−13.6
30	46.01	46.61	1.3	46.01	36.55	−20.6	24.90	31.60	26.9	24.90	24.99	0.4
40	36.78	39.90	8.5	36.78	32.27	−12.2	20.00	27.17	35.8	20.00	22.10	10.5
	T_{exp} (K)	T_{mix} (K)	ε (%)	T_{exp} (K)	T_{mix} (K)	ε (%)	T_{exp} (K)	T_{mix} (K)	ε (%)	T_{exp} (K)	T_{mix} (K)	ε (%)
4.8	300.61	302.57	0.7	300.61	293.32	−2.4	280.41	285.11	1.7	280.41	277.05	−1.2
10.8	294.93	298.07	1.1	294.93	287.16	−2.6	275.79	281.29	2.0	275.79	271.81	−1.4
16.8	291.06	293.49	0.8	291.06	282.38	−3.0	270.94	277.30	2.3	270.94	267.67	−1.2
22.8	286.90	289.27	0.8	286.90	278.70	−2.9	266.85	273.62	2.5	266.85	264.43	−0.9
28.8	282.81	285.33	0.9	282.81	275.57	−2.6	265.06	270.17	1.9	265.06	261.65	−1.3
34.8	280.55	281.57	0.4	280.55	272.65	−2.8	262.39	266.88	1.7	262.39	259.05	−1.3
40.8	277.52	277.86	0.1	277.52	269.93	−2.7	259.27	263.60	1.7	259.27	256.62	−1.0
46.8	272.84	273.96	0.4	272.84	267.40	−2.0	254.63	260.13	2.2	254.63	254.36	−0.1
52.8	265.72	269.20	1.3	265.72	265.05	−0.3	248.36	255.70	3.0	248.36	252.27	1.6

This is a preprint of the following article: Romei, A., & Persico, G., *Computational fluid-dynamic modelling of two-phase compressible flows of carbon dioxide in supercritical conditions*, Appl. Therm. Eng., 2021.
The published article may differ from this preprint, and is available at: 10.1016/j.applthermaleng.2021.116816

Table A.8: Comparison of numerical predictions against experiments [9] for condensing expansions.

	Case 1			**Case 2**			**Case 3**			**Case 4**			**Case 5**		
x (mm)	P_{exp} (bar)	P_{mix} (bar)	ε (%)	P_{exp} (bar)	P_{mix} (bar)	ε (%)	P_{exp} (bar)	P_{mix} (bar)	ε (%)	P_{exp} (bar)	P_{mix} (bar)	ε (%)	P_{exp} (bar)	P_{mix} (bar)	ε (%)
−28	58.08	58.02	0.1	64.38	64.36	0.0	72.44	72.46	0.0	78.77	78.88	0.1	83.47	83.63	0.2
−21	57.48	57.13	−0.6	63.85	63.41	−0.7	71.97	71.44	−0.7	78.46	77.84	−0.8	82.80	82.59	−0.3
−14	54.97	54.38	−1.1	61.14	60.53	−1.0	68.89	68.36	−0.8	75.94	74.70	−1.6	80.49	79.48	−1.3
−7	48.40	47.10	−2.7	54.01	53.08	−1.7	62.67	60.57	−3.3	69.42	66.98	−3.5	74.10	72.05	−2.8
0	34.54	33.08	−4.2	41.12	40.40	−1.8	52.24	46.04	−11.9	53.96	50.68	−6.1	57.99	54.54	−5.9
7	32.82	28.64	−12.7	39.41	33.14	−15.9	42.11	37.84	−10.1	45.90	41.83	−8.9	49.71	45.28	−8.9
14	29.89	26.14	−12.5	35.48	29.97	−15.5	38.11	34.28	−10.1	41.90	37.95	−9.4	45.35	41.17	−9.2
21	28.01	24.20	−13.6	32.91	27.65	−16.0	35.81	31.65	−11.6	39.71	35.09	−11.6	43.03	38.12	−11.4
28	25.87	22.57	−12.8	30.07	25.77	−14.3	32.74	29.53	−9.8	36.07	32.77	−9.1	38.95	35.64	−8.5
35	23.51	21.22	−9.7	27.31	24.20	−11.4	29.84	27.73	−7.1	32.99	30.81	−6.6	35.58	33.55	−5.7
42	21.89	20.03	−8.5	25.28	22.83	−9.7	27.63	26.18	−5.3	30.55	29.10	−4.7	32.90	31.72	−3.6
49	20.59	18.98	−7.8	23.75	21.63	−8.9	25.89	24.80	−4.2	28.63	27.59	−3.6	30.91	30.09	−2.6
56	19.50	18.24	−6.5	22.43	20.78	−7.3	24.39	23.84	−2.3	26.92	26.53	−1.5	28.98	28.94	−0.1

This is a preprint of the following article: Romei, A., & Persico, G., *Computational fluid-dynamic modelling of two-phase compressible flows of carbon dioxide in supercritical conditions*, Appl. Therm. Eng., 2021.
The published article may differ from this preprint, and is available at: 10.1016/j.applthermaleng.2021.116816

References

[1] G. Lorentzen, Revival of carbon dioxide as a refrigerant, International Journal of Refrigeration 17 (5) (1994) 292 – 301. doi:10.1016/0140-7007(94)90059-0.

[2] S. Elbel, N. Lawrence, Review of recent developments in advanced ejector technology, International Journal of Refrigeration 62 (2016) 1 – 18. doi:10.1016/j.ijrefrig.2015.10.031.

[3] G. Angelino, Carbon Dioxide Condensation Cycles For Power Production, Journal of Engineering for Power 90 (3) (1968) 287–295. doi:10.1115/1.3609190.

[4] E. Feher, The supercritical thermodynamic power cycle, Energy Conversion 8 (2) (1968) 85 – 90. doi:10.1016/0013-7480(68)90105-8.

[5] V. Dostal, A supercritical carbon dioxide cycle for next generation nuclear reactors, Ph.D. thesis, Massachusetts Institute of Technology (2004).

[6] F. Crespi, G. Gavagnin, D. Sanchez, G. S. Martinez, Supercritical carbon dioxide cycles for power generation: A review, Applied Energy 195 (2017) 152–183. doi:10.1016/j.apenergy.2017.02.048.

[7] G. Musgrove, S. Wright, 1 - Introduction and background, in: K. Brun, P. Friedman, R. Dennis (Eds.), Fundamentals and Applications of Supercritical Carbon Dioxide (sCO_2) Based Power Cycles, Woodhead Publishing, 2017, pp. 1 – 22. doi:/10.1016/B978-0-08-100804-1.00001-3.

[8] C. Lettieri, N. D. Baltadjiev, M. Casey, Z. S. Spakovszky, Low-Flow-Coefficient Centrifugal Compressor Design for Supercritical CO_2, Journal of Turbomachinery 136 (8) (2014) 081008. doi:10.1115/1.4026322.

[9] C. Lettieri, D. Paxson, Z. Spakovszky, P. Bryanston-Cross, Characterization of Nonequilibrium Condensation of Supercritical Carbon Dioxide in a de Laval Nozzle, Journal of Engineering for Gas Turbines and Power 140 (4) (2017) 041701. doi:10.1115/1.4038082.

[10] Y. Bartosiewicz, Modeling of two-phase choked flows, in: S. Chabane, J.-M. Buchlin (Eds.), Flow Characteristics and performance of safety valves. Lecture Series 2013-08, Von Karman Institute for Fluid Dynamics, 2013.

[11] D. Tan, Y. Li, I. Wilkes, E. Vagnoni, R. L. Miorini, J. Katz, Experimental investigation of the role of large scale cavitating vortical structures in performance breakdown of an axial waterjet pump, Journal of Fluids Engineering 137 (111301) (2015). doi:10.1115/1.4030614.

[12] R. Diener, J. Schmidt, Sizing of throttling device for gas/liquid two-phase flow Part 1: Safety valves, Process Safety Progress 23 (2004) 335–344. doi:10.1002/prs.10034.

[13] R. Diener, J. Schmidt, Sizing of throttling device for gas/liquid two-phase flow Part 2: Control valves, orifices, and nozzles, Process Safety Progress 24 (2005) 29–37. doi:10.1002/prs.10035.

[14] A. Hosangadi, V. Ahuja, Numerical Study of Cavitation in Cryogenic Fluids , Journal of Fluids Engineering 127 (2) (2005) 267–281. doi:10.1115/1.1883238.

[15] J. Zhu, S. Wang, X. Zhang, Influences of thermal effects on cavitation dynamics in liquid nitrogen through venturi tube, Physics of Fluids 32 (1) (2020) 012105. doi:10.1063/1.5132591.

[16] J. B. Young, Two-dimensional, nonequilibrium, wet-steam calculations for nozzles and turbine cascades, Journal of Turbomachinery 114 (1992) 569–579. doi:10.1115/1.2929181.

[17] M. Grübel, J. Starzmann, M. Schatz, T. Eberle, D. Vogt, F. Sieverding, Two-Phase Flow Modeling and Measurements in Low-Pressure Turbines - Part I: Numerical Validation of Wet Steam Models and Turbine Modeling, Journal of Engineering for Gas Turbines and Power 137 (042602) (2015). doi:10.1115/1.4028468.

[18] M. Schatz, T. Eberle, M. Grübel, J. Starzmann, D. Vogt, N. Suerken, Two-Phase Flow Modeling and Measurements in Low-Pressure Turbines - Part II: Turbine Wetness Measurement and Comparison to Computational Fluid Dynamics-Predictions, Journal of Engineering for Gas Turbines and Power 137 (042603) (2015). doi:10.1115/1.4028547.

This is a preprint of the following article: Romei, A., & Persico, G., *Computational fluid-dynamic modelling of two-phase compressible flows of carbon dioxide in supercritical conditions*, Appl. Therm. Eng., 2021.
The published article may differ from this preprint, and is available at: 10.1016/j.applthermaleng.2021.116816

[19] C. E. Brennen, Homogeneous flows, in: Fundamentals of Multiphase Flow, Cambridge University Press, 2005, pp. 176–198. doi:10.1017/CBO9780511807169.010.

[20] G. Gyarmathy, Nucleation of steam in high-pressure nozzle experiments, Proceedings of the Institution of Mechanical Engineers, Part A: Journal of Power and Energy 219 (6) (2005) 511–521. doi:10.1243/095765005X31388.

[21] M. De Lorenzo, P. Lafon, J.-M. Seynhaeve, Y. Bartosiewicz, Benchmark of delayed equilibrium model (dem) and classic two-phase critical flow models against experimental data, International Journal of Multiphase Flow 92 (2017) 112 – 130. doi:10.1016/j.ijmultiphaseflow.2017.03.004.

[22] Y. Bartosiewicz, Z. Aidoun, Y. Mercadier, Numerical assessment of ejector operation for refrigeration applications based on cfd, Applied Thermal Engineering 26 (5-6) (2006) 604–612. doi:10.1016/j.applthermaleng.2005.07.003.

[23] Q. Dang Le, R. Mereu, G. Besagni, V. Dossena, F. Inzoli, Computational Fluid Dynamics Modeling of Flashing Flow in Convergent-Divergent Nozzle, Journal of Fluids Engineering 140 (10), 101102 (05 2018). doi:10.1115/1.4039908.

[24] M. Palacz, J. Smolka, A. Fic, Z. Bulinski, A. J. Nowak, K. Banasiak, A. Hafner, Application range of the HEM approach for CO2 expansion inside two-phase ejectors for supermarket refrigeration systems, International Journal of Refrigeration 59 (2015) 251 – 258. doi:10.1016/j.ijrefrig.2015.07.006.

[25] F. Giacomelli, F. Mazzelli, A. Milazzo, A novel cfd approach for the computation of r744 flashing nozzles in compressible and metastable conditions, Energy 162 (2018) 1092 – 1105. doi:10.1016/j.energy.2018.08.050.

[26] A. Hosangadi, Z. Liu, T. Weathers, V. Ahuja, J. Busby, Modeling Multiphase Effects in CO2 Compressors at Subcritical Inlet Conditions, Journal of Engineering for Gas Turbines and Power 141 (8) (03 2019). doi:10.1115/1.4042975.

[27] J. Bodys, J. Smolka, M. Palacz, M. Haida, K. Banasiak, Non-equilibrium approach for the simulation of co2 expansion in two-phase ejector driven by subcritical motive pressure, International Journal of Refrigeration 114 (2020) 32 – 46. doi:10.1016/j.ijrefrig.2020.02.015.

[28] M. Pini, A. Spinelli, G. Persico, S. Rebay, Consistent look-up table interpolation method for real-gas flow simulations, Computers & Fluids 107 (2015) 178 – 188. doi:10.1016/j.compfluid.2014.11.001.

[29] E. Rinaldi, R. Pecnik, P. Colonna, Computational fluid dynamic simulation of a supercritical CO_2 compressor performance map, J. Eng. Gas Turb. Power 137 (7) (2015) 072602. doi:10.1115/1.4029121.

[30] A. Ameli, A. Afzalifar, T. Turunen-Saaresti, J. Backman, Effects of Real Gas Model Accuracy and Operating Conditions on Supercritical CO2 Compressor Performance and Flow Field, Journal of Engineering for Gas Turbines and Power 140 (6), 062603 (01 2018). doi:10.1115/1.4038552.

[31] M. Nakagawa, M. S. Berana, A. Kishine, Supersonic two-phase flow of CO_2 through converging–diverging nozzles for the ejector refrigeration cycle, International Journal of Refrigeration 32 (6) (2009) 1195–1202. doi:10.1016/j.ijrefrig.2009.01.015.

[32] M. Ishii, T. Hibiki, Thermo-Fluid Dynamics of Two-Phase Flow, Springer-Verlag New York, 2011. doi:10.1007/978-1-4419-7985-8.

[33] Y. Fang, Advanced numerical simulations of two-phase CO_2 ejectors, Ph.D. thesis, Universite catholique de Louvain (2019).

[34] F. R. Menter, Two-equation eddy-viscosity turbulence models for engineering applications, AIAA Journal 32 (8) (1994) 1598–1605. doi:10.2514/3.12149.

[35] P. R. Spalart, S. R. Allmaras, A one-equation turbulence model for aerodynamic flows, AIAA Paper 92-0439 (1992). doi:10.2514/6.1992-439.

[36] G. J. Otero R., A. Patel, R. Diez S., R. Pecnik, Turbulence modelling for flows with strong variations in thermo-physical properties, International Journal of Heat and Fluid Flow 73 (2018) 114 – 123. doi:10.1016/j.ijheatfluidflow.2018.07.005.

[37] J. Young, The condensation and evaporation of liquid droplets in a pure vapour at arbitrary knudsen number, International

Journal of Heat and Mass Transfer 34 (7) (1991) 1649 – 1661. doi:10.1016/0017-9310(91)90143-3.

[38] R. Span, W. Wagner, A new equation of state for carbon dioxide covering the fluid region from the triplepoint temperature to 1100 k at pressures up to 800 mpa, Journal of Physical and Chemical Reference Data 25 (6) (1996) 1509–1596. doi:10.1063/1.555991.

[39] M. De Lorenzo, P. Lafon, M. Di Matteo, M. Pelanti, J.-M. Seynhaeve, Y. Bartosiewicz, Homogeneous two-phase flow models and accurate steam-water table look-up method for fast transient simulations, International Journal of Multiphase Flow 95 (2017) 199 – 219. doi:10.1016/j.ijmultiphaseflow.2017.06.001.

[40] G. Persico, P. Gaetani, A. Romei, L. Toni, E. Bellobuono, R. Valente, Implications of phase change on the aerodynamics of centrifucal compressors for supercritical carbon dioxide applications, in: Proceedings of the ASME Turbo Expo 2020, no. GT2020-14988, 2020, pp. 1–12. doi:10.1115/GT2020-14988.

[41] K. Banasiak, A. Hafner, Mathematical modelling of supersonic two-phase R744 flows through convergingdiverging nozzles: The effects of phase transition models, Applied Thermal Engineering 51 (1) (2013) 635 – 643. doi:10.1016/j.applthermaleng.2012.10.005.

[42] T. Adams, C. Grant, H. Watson, A simple algorithm to relate measured surface roughness to equivalent sand-grain roughness, nternational Journal of Mechanical Engineering and Mechatronics 1 (2012) 66–71. doi:10.11159/ijmem.2012.008.

[43] P. J. Roache, Quantification of uncertainty in computational fluid dynamics, Annual Review of Fluid Mechanics 29 (1) (1997) 123–160. doi:10.1146/annurev.fluid.29.1.123.

[44] T. Flatten, H. Lund, Relaxation two-phase flow models and the subcharacteristic condition, Mathematical Models and Methods in Applied Sciences 21 (12) (2011) 2379–2407. doi:10.1142/S0218202511005775.

[45] M. Pelanti, K. Shyue, A numerical model for multiphase liquid–vapor–gas flows with interfaces and cavitation, International Journal of Multiphase Flow 113 (2019) 208 – 230. doi:10.1016/j.ijmultiphaseflow.2019.01.010.

[46] A. B. Wood, A textbook of sound: being an account of the physics of vibrations with special reference to recent theoretical and technical developments, New York: The Macmillan company, 1941.

[47] P. A. Thompson, A fundamental derivative in gasdynamics, Physics of Fluids 14 (9) (1971) 1843–1849. doi:10.1063/1.1693693.

[48] N. R. Nannan, A. Guardone, P. Colonna, On the fundamental derivative of gas dynamics in the vapor–liquid critical region of single-component typical fluids, Fluid Phase Equilibria 337 (2013) 259–273. doi:10.1016/j.fluid.2012.09.017.

[49] P. A. Thompson, K. C. Lambrakis, Negative shock waves, Journal of Fluid Mechanics 60 (1973) 187–208. doi:10.1017/S002211207300011X.

[50] M. Yazdani, A. A. Alahyari, T. D. Radcliff, Numerical modeling of two-phase supersonic ejectors for work-recovery applications, International Journal of Heat and Mass Transfer 55 (21) (2012) 5744 – 5753. doi:10.1016/j.ijheatmasstransfer.2012.05.071.